Millimeter-Wave Base Stations in the Sky: An Experimental Study of UAV-to-Ground Communications

Sara Garcia Sanchez, Subhramoy Mohanti, Dheryta Jaisinghani, *Member, IEEE*, and Kaushik Roy Chowdhury, *Senior Member, IEEE*

Abstract—This paper adopts a systems approach to study how millimeter wave (mmWave) radio transmitters on UAVs provide high throughput links under typical hovering conditions. With Terragraph channel sounder units, we experimentally study the impact of signal fluctuations and sub-optimal beam selection on a testbed involving DJI M600 UAVs. From the hovering-related insights and the measured antenna radiation patterns, we develop and validate the first stochastic UAV-to-Ground mmWave channel model with UAVs as transmitters. Our UAV-centric analytical model complements the classical fading with additional losses expected in the mmWave channel during hovering, considering 3-D antenna configuration and beamforming training parameters. We specifically consider lateral displacement, roll, pitch, and yaw, whose magnitude vary depending on the availability of specialized hardware such as real-time kinematic GPS. We then leverage this model to mitigate the hovering impact on the UAV-to-Ground link by selecting a near-to-optimum pair of beams. Importantly, our work does not change the wireless standard nor require any cross-layer information, making it compatible with current mmWave devices. Results demonstrate that our channel model drops estimation error to $\approx$ 0.2 percent, i.e., 18x lower, and improves the average PHY bit-rate by $\approx$ 10 percent when compared to existing state-of-the-art channel models and beamforming methods for UAVs.

Index Terms—mmWave, hovering, UAV-to-Ground, channel model,beam selection

1 Introduction

The acute spectrum scarcity in the desirable sub-6 GHz frequency band has spurred interest in mmWave bands, where substantial amount of untapped channel resources exist [1]. While extensive investigation has been conducted on the particularities of these higher frequencies, the Federal Communications Commission (FCC) is creating new opportunities for the next generation of WiFi in the above-95 GHz band. This has placed mmWave frequencies as a potential candidate to provide high throughput service through the next generation WiFi and 5G standards [2]. Furthermore, from the usage point of view, wireless capacity demand exhibits high spikes of short duration at locations where existing infrastructure may not be sufficient. This makes permanent deployments too costly, forcing to find flexible solutions to cover temporary additional needs. Thus, (i) obtaining a fundamental understanding of the practical constraints of operating in the mmWave bands, as well as (ii) addressing the limitations of static transceiver infrastructure, are salient to realizing a viable mmWave based system [3]. As a possible solution, we envisage a network architecture of UAVs mounted with digitally steerable mmWave antennas, serving as aero mobile base stations, that can be flexibly positioned in time and space.

- *Motivation for mmWave-enabled UAV deployment*: Given the high capital investment in installing mmWave equipment, static urban deployment must carefully consider cost-benefit tradeoffs, especially when traffic spikes occur at different locations and times. For example, train/bus stations, sporting venues, coffee shops and downtown offices exhibit short-term capacity shortfalls that coincide with human activity patterns [4]. To address these scenarios, UAVs with on-board mmWave radios can be continuously moved to serve pockets of users [5], [6], [7], [8]. In the absence of optical fiber, UAVs rely on point to point mmWave backhaul links to the nearest fixed tower, while serving users on ground (ground nodes) with the desired mmWave cellular or WiFi standard. For our experimental mmWave-enabled UAV channel modeling and beam selection optimization, we have chosen COTS 802.11ad hardware, though our work is applicable to any other mmWave capable WiFi/cellular standard of interest.
- *Challenges in mmWave-enabled UAVs*: Current mmWave standards use beamforming to create constructive signal addition at the receiver [9], [10]. While beamforming helps combat additional losses due to higher sensitivity to rain/gas absorption and the use of smaller antenna apertures, compared to lower frequencies [11], [12], narrowly directing energy may cause frequent antenna beam misalignments due to the continuous hovering-related UAV displacements. In Fig. 1, we visualize the implications of the term *hovering* as the total sum of various motion artifacts, including

- *The authors are with the Institute for the Wireless Internet of Things, Northeastern University, Boston, MA 02115 USA. E-mail: {sgarcia, smohanti}@coe.neu.edu, {dheryta, krc}@ece.neu.edu.*

Manuscript received 25 Nov. 2019; revised 5 June 2020; accepted 27 July 2020. Date of publication 3 Aug. 2020; date of current version 7 Jan. 2022. (Corresponding author: Sara Garcia Sanchez.) Digital Object Identifier no. 10.1109/TMC.2020.3013575

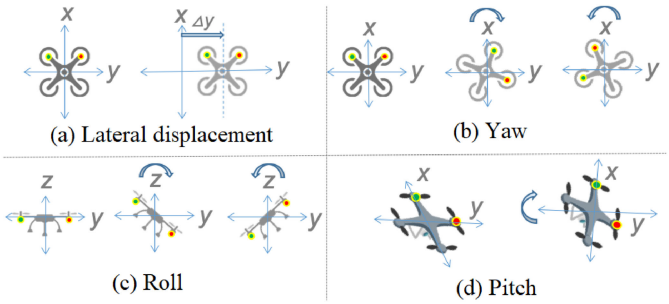

Fig. 1. (a) UAV movement with lateral displacement (shown only for y axis), (b) yaw (along x-y plane), (c) roll (around x axis), and (d) pitch (nose moves upwards, leaving x-y plane).

translational motion along three axes, and rotational motion - yaw, roll, and pitch. These types of motion during hovering are caused by the in-built GPS module localization inaccuracy, and follow a Gaussian distribution [13] that can extend up to $\pm 1.5m$ along any single axis in the horizontal plane and $\pm 0.5m$ along the vertical axis within the 3-D space [14], being even larger for less stable UAVs models. In addition to beam misalignment, UAV motion during hovering may lead to an undesirable situation in which the pair of beams chosen by conventional beam selection techniques presents sub-optimal performance over time. We demonstrate this problem in Fig. 2, with actual measured data of the unpredictable UAV displacements. As shown in Fig. 2 (left), when the transmitter and receiver radios are static, the pair of beams selected after beam-sweeping is optimum, resulting in a perfect match over time. However, with hovering UAVs as mmWave transmitters, in Fig. 2 (right), the UAV location fluctuates. As a result of this, the UAV does not statically stay at its initial location, but rather moves from one location to another within the hovering displacement range. Moreover, from our experimental observations, there is no guarantee that when beam-sweeping is performed, the UAV location (*Location 1* in Fig. 2), corresponds to the center of the hovering Gaussian distribution (*Location 2* in Fig. 2), where the UAV is most likely to be over time. In this case, the selected pair of beams, which was optimum in *Location 1*, turns out to be sub-optimal in average as the UAV location changes and beams become misaligned. The combination of beam misalignment and sub-optimal beam selection eventually lead to received power fluctuations and decreased average performance over time, highly degrading the communication link.

• *Summary of Contributions*:

Current UAV-to-Ground mmWave channel models are idealistic and limited in their abilities to capture practical effects caused by the UAV airframe and its hovering-related motion. A key unsolved challenge that we tackle in this paper is to design and experimentally validate a fine-grained mmWave channel model that complements the classical fading, by specifically taking into account–(i) the UAV airframe and its effect on the mmWave signal propagation and (ii) fading caused by the unique UAV movement patterns shown in Fig. 1. For the latter, based on experimental observations, we prove that besides expected misalignment loss, hovering motion also causes the sub-optimal beam selection problem discussed in Fig. 2. Non-intuitively, guided by our channel model, our work also

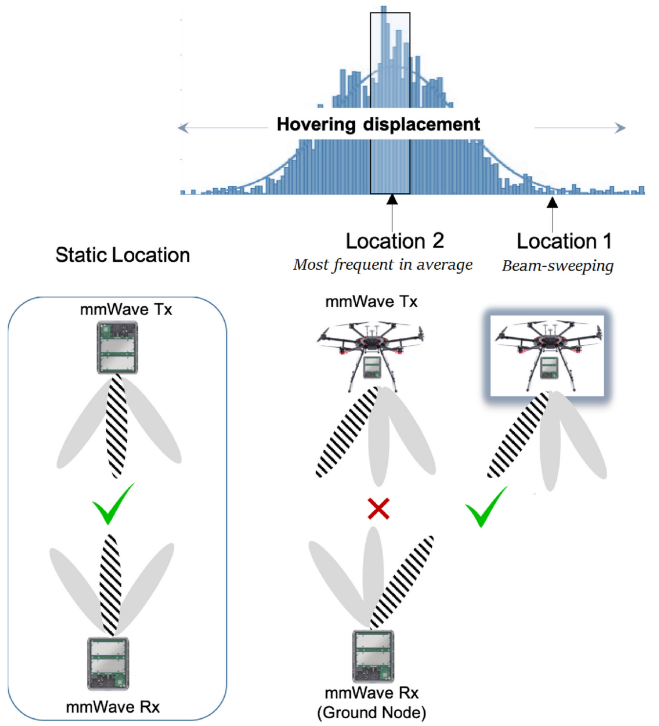

Fig. 2. Sub-optimal beam selection under hovering.

demonstrates that choosing specific sub-optimal beams after beam-sweeping, improves the average performance of the UAV mmWave-link over time, compared to the existing standard. Towards this aim, we design an algorithm that optimizes the beam selection for mmWave-enabled UAV transmitters, such that the average SNR at the receiver maximizes over time. To summarize, our work adopts a rigorous systems-approach, by making the following contributions:

1) We identify and empirically characterize the significant effect of the UAV airframe and the sub-optimal beam selection problem in existing standards using 802.11ad complaint Terragraph radios, in Section 3. In addition, we quantitatively relate these two effects, as well as beam misalignment caused by hovering with, (i) additional fading and (ii) resulting power fluctuations over time, by comparing collected data from static and UAV-to-Ground links.
2) We build and experimentally validate the first stochastic analytical UAV-to-Ground channel model that takes a systems-approach to estimate additional fading in mmWave links, complementing existing models, in Section 4. In particular, our model includes the effects of UAV translational motion along the three axes, as well as yaw, pitch, and roll characterized from experimental data. Following the acceptance of the paper, the hovering raw data trace-files will be released to the community. Our model also considers the dependence on 3-D radiation patterns of the highly directional antennas, measured under actual flying conditions and potential vibrations. Moreover, and for the first time, we include the effect of a potential sub-optimum beam selection

in the fading estimation. Lastly, we tailor our model to different deployment parameters, hovering conditions, and beamforming training configurations, such as the beam-sweeping angular resolution and maximum angular range.

3) In order to overcome the problem of sub-optimal beam selection, we propose a standards-compliant approach that selects a near-to-optimum pair of beams for given hovering conditions and antenna radiation patterns, in Section 5. Moreover, our approach utilizes hovering data collected in-situ during actual flight, without using a dedicated time-slot for data collection. We compare our algorithm performance with the standard-based approach during UAV experiments in Section 6, where we also validate our channel model using measured data during flight and show its superior accuracy compared to prevalent idealistic models.

2 Related Work

• *Channel Modelling Efforts:* There has been a significant effort to understand and characterize mmWave channels in different scenarios over the last few years, including indoor [15], [16], urban [17] and rural environments [18]. The work in [19] presents an overview of channel modeling efforts from several international groups, who propose models for Line-of-Sight (LOS) probability, path loss and building penetration through extensive research and measurement campaigns. Specific to mobility, for Vehicle-to-Infrastructure (V2I) communications, the authors in [17] characterize the channel for an urban environment through simulations in the 28 GHz frequency band. For Vehicle-to-Vehicle (V2V) communications, an empirical characterization for large and small scale fading is performed in [20], whereas [21] analyzes the effect of small vibrations on the doppler spread. However, none of these works involve UAVs as part of the communication system.

For UAV communications, the works in [22], [23], [24], [25] survey and discuss channel model involving UAVs for the Air-to-Ground link. [22] presents a measurement campaign for both narrow and wide bandwidths, performed in a suburban environment; while [23] proposes a statistical model based on ultrawideband channel sounding. More recently, the authors in [26] and [27] characterize the UAV-to-ground channel in LOS and NLOS urban environments through ray tracing simulations, whereas in [28], the authors propose and validate through empirical analysis their proposed Air-to-Ground channel model, without including the unique UAV structural characteristics and hovering motion patterns. However, all these works are developed for the sub-6 GHz band, and thus, their outcomes cannot be generalized for higher mmWave frequencies. In contrast, in this work we provide a model to estimate UAV-related fading, applied to a 60 GHz mmWave link that can be generalized to other frequency bands. Although there exist works on channel modeling for UAV-based mmWave links, they lack experimental validation and most of them do not include the UAV dynamics into the model. For instance in [29], the authors use ray-tracing simulations to model the air-to-ground channels in 28 GHz and 60 GHz, whereas in [30], a stochastic geometry based 3-D model that considers the directionality and the random heights of transmitters and receivers is proposed. We instead include the UAV motion patterns modelled from collected data during actual flights, and experimentally validate our approach. The closest work found in the literature is presented in [31]. Here, the authors consider additional losses due to the UAV hovering motion, though their model lacks a straightforward relationship with UAV flying parameters and beamforming training configuration. Moreover, they assume an ideal antenna radiation pattern, limiting their analysis to the main lobe. Lastly, their proposed model is validated with simulations; thus, lacking experimental validation. We show how some of these assumptions may lead to inaccuracies in the theoretical model when compared to actual experimental data.

• *beam selection Algorithms:* There exist several works aiming to optimize the process of beam selection. In [32] the authors find the optimal steering direction on IEEE 802.11ad compatible devices, accounting for measured radiation patterns and sweeping only through a subset of probing sectors. InferBeam [33], proposes to model the environment as a 3D grid and use Conditional Random Field to map every discrete point to an optimal antenna sector. In [34] the authors track the channel dynamics to find the best beam under mobility. 3D scene reconstruction has been proposed in [35] from surrounding images of a given user, which is used to train a deep neural network, to predict the optimal mmWave transmit and receive beam indices. The authors in [36] estimate the power delay profile of a sub-6 GHz channel, as inputs for a deep neural network to predict the optimal mmwave beam, bypassing the traditional beam sweeping process. Whereas in [37], the authors propose to learn the optimal beam pair index by exploiting the locations and types of the receiver vehicle and its neighboring vehicles (situational awareness), leveraging machine learning classification and past beam training data. However, none of the existing works identify and address the sub-optimal beam selection problem, in particular to hovering UAVs, which we tackle here. To the best of our knowledge, we are the first to provide a robust channel model for mmWave-enabled UAVs that accurately estimates additional fading induced as an effect of realistic antenna radiation patterns, displacement due to UAV hovering, and sub-optimal beam selection. Also, we provide a near-to-optimum beam selection which enhances the average performance under hovering conditions.

3 Study of UAV Hovering in mmWave Links

We first present our hardware selection in Section 3.1. Then, we experimentally characterize the effect of the UAV airframe and the UAV motion during hovering illustrated in Fig. 1, on additional fading compared to static links, in Sections 3.2 and 3.3. Finally, based on our empirical results, we motivate the need for a tailored UAV-to-Ground channel model and improved beam selection algorithm for hovering scenarios, in Section 3.4.

3.1 Hardware Selection

1) *MmWave Sounders.* We use Terragraph (TG) channel sounders, a customized pair of nodes from Facebook [38]. They are designed for the channel modeling of

60 GHz links, with capability to measure directional path loss, Signal-to-Noise Ratio (SNR) at the receiver and physical (PHY)-bitrate, among other parameters. Their maximum Effective Isotropic Radiated Power (EIRP) is 45 dBm. Each TG sounder antenna consists of a phased array composed of 36×8 radiating elements. All radiating elements in a given column are connected to the same phase shifter, and thus, steering is not supported in the elevation plane (φ). In the azimuth plane (θ), the steering angular range is $[-45°, 45°]$. Azimuth steering is performed using pre-calibrated antenna weight vectors (AWVs). However, in the existing version of the TG sounders, AWVs cannot be customized, and beam steering is instead achieved using a set of 64 predefined beams. Each predefined beam is a steered version of a uniformly illuminated array. The antenna 3-dB beamwidth (θ_{3dB}) can be set to $2.8°$, $8.5°$, and $105°$. The TG sounders implement the PHY layer of 802.11ad protocol, consisting of 58.32, 60.48 and 62.64 GHz frequency bands and MCS of 1 - 12. In 802.11ad, the communicating nodes agree on the optimal pair of transmit and receive beams to maximize signal quality and throughput. This process, referred to as *beamforming training*, takes advantage of the discretized antenna azimuth that reduces the search space of possible antenna array configurations. In the standard, after a first sector matching, a second beam-sweeping stage allows further refinement within the selected sectors. TG sounders skip the first sector matching of the 802.11ad beam selection process, and only perform the refinement stage among the set of predefined beams.

2) *UAV model.* Given the total weight (12 Kg) including external modules–the channel sounder and positioning system–, the DJI-M600 is the only apt choice for us, as it can carry weights up to 15 Kg. The UAV is equipped with an in-built GPS module to determine its location and take required actions to reach its targeted coordinates. However, classical in-built GPS module introduces an error of ≈ 0.7 m and up to 1.5 m in the measured location. Thus, when a UAV is programmed to hover at certain targeted coordinates, it experiences a continuous motion around them, as it relies on inaccurate GPS signals for localization. Given this, we also equip the UAV with an RTK-GPS [39], mounted on the M600 as an add-on module and provides a near-stable UAV location measurement with ≈ 0.1 m variation. However, this enhanced positioning accuracy effectively doubles the cost of the M600 setup [39], [40] and hence, our experimental study involves both configurations. The UAV is provided with an Inertial Measurement Unit (IMU) for rotational data collection. An onboard NVIDIA Jetson TX2 compute module stores all sensor data during the experiment.

3) *Localization measurement system.* Our proposed beam selection algorithm requires to log the UAV location during flight with high accuracy. Given the high cost of the M600 RTK-GPS add-on module, we do not assume its availability. Instead, we use a low-cost RTK-GPS system, EMLID Reach M+, which also provides cm-level localization accuracy. In our setup, this system is only used for data collection and cannot be directly integrated with the UAV navigation system to modify the UAV flight pattern. Thus, three different localization system are mentioned in this work: GPS or RTK-GPS used for navigation and the low-cost RTK-GPS EMLID Reach M+ with the only purpose of data collection.

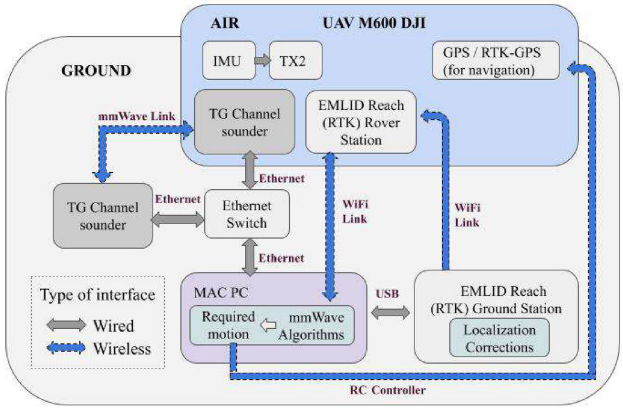

Fig. 3. System diagram for the experimental setup.

In Fig. 3, we present a system diagram showing the interconnection between the aforementioned hardware modules.

3.2 Effect of UAV Airframe on the Antenna Radiation Pattern

It is well-known that mmWave signals present reflective properties to certain types of material, such as metal and hard plastic. Moreover, mmWave signal propagation has been proven to be sensitive to potential vibrations induced by wind bursts [41] or by a lack of perfect synchronization in UAV quad-rotor systems [42]. While the aforementioned reflecting materials are commonly used for UAV manufacturing, vibrations can cause UAV instability and alter the antenna frequency response. For this reason, and given the proximity of the mmWave sounder to the UAV underside (see Fig. 6), we were motivated to study how the UAV airframe and potential vibrations affect signal propagation. In order to analyse this phenomena, we compare the TG sounder antenna radiation pattern measured in a RF anechoic chamber for two different setups–(i) with the transmitter on a tripod and thus, free of surrounding reflecting structure, and (ii) with the transmitter attached to the under-side of a M600 UAV using 3-D printed hardware, as we illustrate in Fig. 6. For the latter setup, the UAV rotors were turned on, in order to account for vibrations and emulate flying conditions as closely as possible. We denote these setups as *static* and *aerial*, respectively. The receiver remained on a tripod in both setups, at a height of 1.5 meters above the ground, 6 meters away from the transmitter. For each setup, we characterized the radiation pattern for the central beam at the transmitter, according to the predefined beams mentioned in Section 3.1. To this extent, we made both TG sounders perfectly face each other, and fixed their central beams for transmission and reception. Then, we rotated the transmitter sounder by angular steps of $1°$, so that the beams were steered away from each

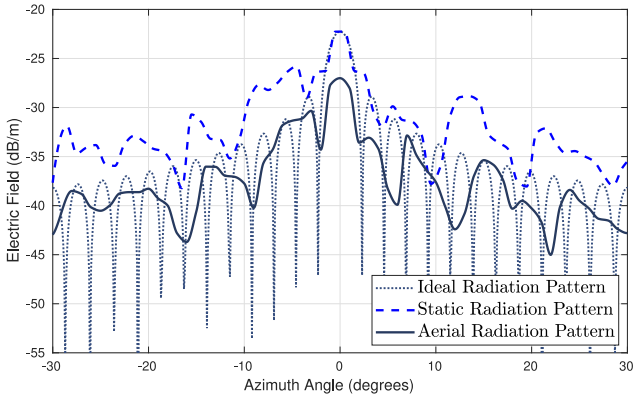

Fig. 4. Antenna radiation pattern under flying conditions.

other at an azimuth angle $\theta \in \mathbb{Z}$ in the range $[-30, 30]$ ($\theta = 0°$, being the perfect alignment). For each position, we logged the link path loss and calculated the electric field from $E(dB/m) = 10log(\sqrt{Z_0 P_d})$, where Z_0 is the free space impedance equal to 120π, and P_d is the power density, computed as $P_d = \frac{gP_r}{4\pi d^2}$, with g the antenna gain, d the distance between transmitter and receiver and P_r the received power calculated as the difference between the EIRP set for transmission and the measured path loss. For validation, we contrasted our characterization for the first setup (tripod case) with TG documentation.

In Fig. 4, we present the measured radiation patterns for both setups, and observe the effect the UAV airframe has on its shape. For reference, we additionally include the *ideal* radiation pattern calculated from antenna array synthesis, for the same beamwidth θ_{3dB} of 2.8° as for the experimental characterization. From the comparison between the *static* and *aerial* radiation patterns, we observe that the UAV hardware and its in-motion rotors cause additional fading L_{Afr} of 9.5 dB, as they perturb the mmWave electric field in the near-field region. Specific values for L_{Afr} depend on the amount of power reflected and scattered on the UAV airframe, given by (i) the UAV airframe shape and material, (ii) the antenna radiation pattern, and (iii) the sounder assembly on the UAV. For our case, since TG sounders do not perform elevation steering, significant amount of power is reflected on the UAV underside, causing large additional fading. Under this observation, theoretical models need to consider potential hardware-mounting related fading in practical deployments.

3.3 Effect of UAV Hovering on the Link Performance

In this section, we aim to experimentally quantify the link performance degradation caused by UAV hovering-related motion, and illustrate its dependency with different deployment and system configuration parameters. To this extent, we first describe in Section 3.3.1 the two direct effects caused by hovering - beam misalignment and potential sub-optimal beam selection -, already introduced in Section 1. Then, in Section 3.3.2, we quantify through experiments how these two phenomena result in power fluctuations and additional fading when compared to static deployments.

3.3.1 Understanding Hovering-Related Effects

First, we illustrate the origin of power fluctuations due to beam misalignment by referring to Fig. 5a. Initially, right after the

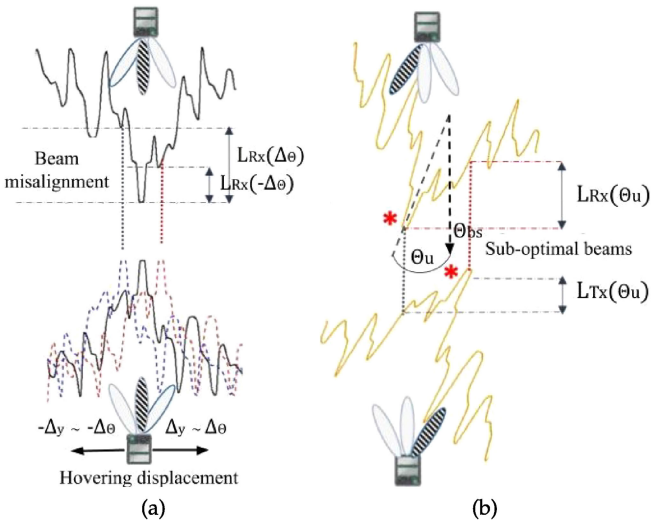

Fig. 5. Illustrating the hovering-related fading caused by (a) beam misalignment and (b) sub-optimal beam selection.

beam-sweeping procedure, transmitter, and receiver beams are perfectly aligned. However, as the transmitter UAV suffers from hovering and experiences displacement from its initial location, its beam becomes misaligned with the receiver's. This causes additional loss L_{Misal} compared to a static setup, as the antenna gains drop. Since the displacement is due to hovering, that is of unpredictable nature, the antenna gains, and consequently L_{Misal}, randomly fluctuate over time. Moreover, the fluctuations magnitude is highly dependent on the antenna radiation patterns and hovering conditions according to Fig. 5a, and increases as the distance between transmitter and receiver is reduced. This highlights the importance of carefully considering hardware features for loss estimation, such as the antenna characteristics and the accuracy of the system used for UAV navigation, which conditions its stability during hovering.

In Fig. 5b, we show the result of sub-optimal beam selection after completing the 802.11ad standard beam-sweeping procedure, caused by the lack of accuracy of the in-built GPS module, as we discussed in Fig. 2. The selection of a sub-optimal pair of beams has two consequences. First, it causes misalignment loss at the center of the hovering displacement range, where the UAV is more likely to be located over time. We denote this loss as L_{SubOpt}, in order to distinguish it from the temporal varying loss discussed in Fig. 5a. Furthermore, as the transmitter hovers under sub-optimal beam conditions in Fig. 5b, the magnitude of the L_{Misal} fluctuations would likely change, as the displacement of UAV would produce misalignment along different regions of the radiation patterns compared to the case in Fig. 5a, causing the antenna gains to also vary on a different range of values. This fact reveals the dependence of L_{Misal} with the selection of a particular pair of beams after beam-sweeping, highlighting the need to jointly consider both effects. The selection of a certain pair of beams is determined by the UAV hovering conditions, distance between transmitter and receiver and antenna radiation patterns. In addition, it also depends on the beamforming training parameters, which determine the angular direction to which transmitter and receiver steer their beams during beam-sweeping.

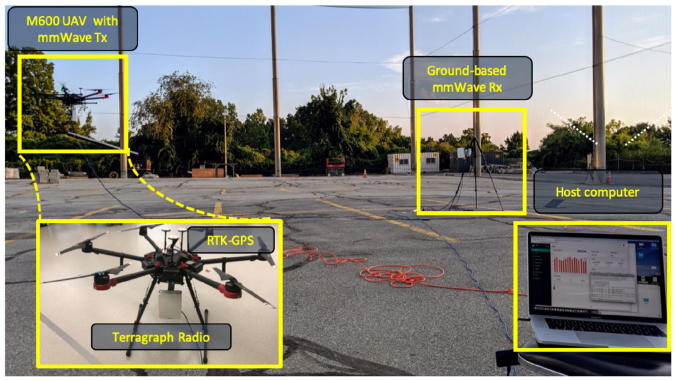

Fig. 6. Experimental setup and close-up view of M600 (inset) with TG sounder and RTK-GPS unit.

3.3.2 Quantifying Hovering Effect on Link Performance

In order to quantify the effect of hovering-related loss on the link performance, we conduct a set experiments. We consider three scenarios experiencing different degree of hovering: a static Ground-to-Ground link, a UAV-to-Ground link where the UAV navigation system relies on an in-built GPS localization module, and the same UAV-to-Ground link where the GPS is replaced by an RTK-GPS module, for increased localization accuracy, as we discussed in Section 3.1. We show our experimental setup in Fig. 6 for the UAV-to-Ground case. It consists of a 802.11ad compliant TG sounder unit mounted on a DJI-M600 UAV operating as a transmitter and another TG sounder unit mounted on a tripod operating as the ground receiver. For the Ground-to-Ground link, both sounders are mounted on tripods. For these experiments, we collect link path loss and SNR by connecting the transmitter and receiver sounder units to a host computer through Ethernet links, as illustrated in Fig. 3, which are long enough so that we do not compromise the UAV natural hovering pattern. We fix the beamwidth θ_{3dB} to the narrowest achievable by TG sounders with its current firmware of 2.8°, motivated by a longer communication range compared to wider beamwidths. However, the general trends can be extrapolated to other beamwidths. As the overlay protocol used is 802.11ad, the best transmitter-receiver beams are automatically selected as per the standard.

In Fig. 7a we show the path loss collected over time for all three scenarios considered. These measurements capture the cumulative fading arising from the two hovering-related effects discussed in Section 3.3.1, as well as the fading caused by the UAV airframe quantified in Section 3.2, none of which apply to the static Ground-to-Ground case. We first observe that the path loss for the UAV-to-Ground link using RTK-GPS only differs from the static case by a magnitude equivalent to the measured airframe fading of 9.5 dB. This is due to the scarce hovering experienced by the UAV when its navigation system relies on RTK-GPS, which limits the severity of power fluctuations caused by beam misalignment, as well as the chances for sub-optimal beam selection after beam-sweeping completion. In order to prove that the observed power fluctuations are due to beam misalignment, we rely on the knowledge of the antenna radiation pattern. We observe that for a typical maximum hovering translational displacement along y-axis Δ_y and for a given distance between transmitter and receiver d, we can determine the maximum angular displacement in the azimuth dimension $\Delta_\theta = atan\frac{\Delta_y}{d}$. Then, from the antenna radiation pattern, we can estimate the gain fluctuation within the range $[-\Delta_\theta, \Delta_\theta]$, which is bounded by 6 dB for the RTK-GPS case, where $\Delta_y \approx 0.1$ m and $d = 6m$ in our setup. We observe that the gain fluctuation matches the experimental power fluctuation magnitude in Fig. 7a. Notice that fading is aggravated when the UAV relies on GPS for navigation and thus, suffers from worse hovering conditions. In this case, the fluctuating path loss values collected during the entire experiment time are bounded by 14 dB, which also matches our estimation based on the antenna radiation pattern. Moreover, these fluctuations are at least 15 dB above the case using RTK-GPS. Therefore, we associate this loss gap to the direct consequence of a sub-optimal beam selection, as choosing a specific pair of beams determines the region of the radiation pattern along which the UAV hovering causes beam misalignment, which may lead to the case in which sub-optimal pairs never reach perfect alignment. These results confirm our hypothesis that the navigation system lack of accuracy causes hovering, eventually leading to increased fading compared to static setups.

In Fig. 7c we show the Empirical Cumulative Distribution Function (ECDF) of the measured SNR for the same experiment and all three scenarios considered. The SNR for

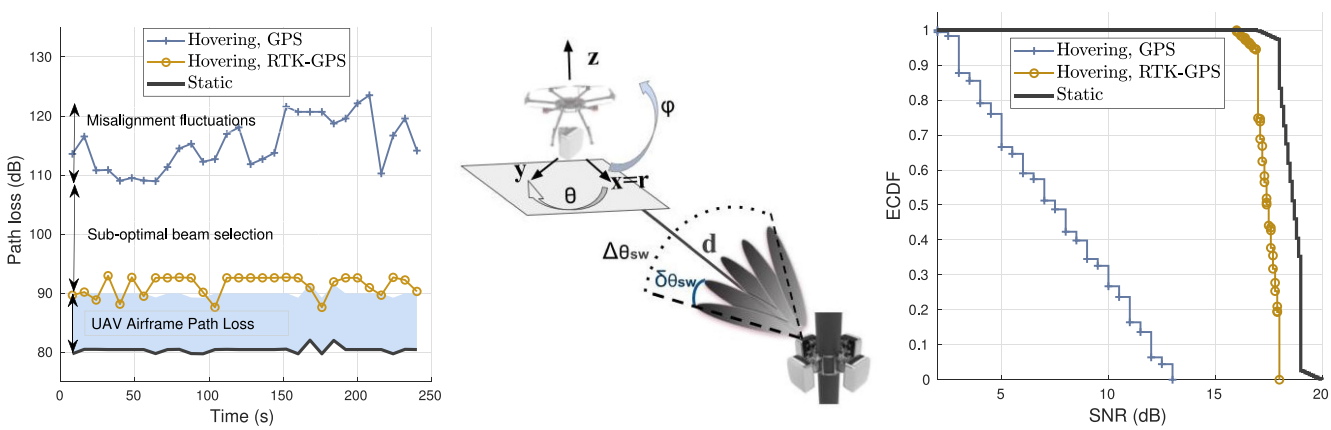

(a) Path loss over time (b) Coordinate systems reference (c) ECDF of SNR

Fig. 7. Showing (a) effect of hovering-related losses on the link performance compared to a static case, (b) polar and Cartesian coordinate systems and beamforming training parameters and (c) SNR drop caused by hovering.

TABLE 1
SNR (dB) for Different Confidence Levels

Type of Link	25%	50%	75%
Ground-Ground (Static)	18.2	18.7	19
UAV-Ground (Hovering, GPS)	17	17.4	17.9
UAV-Ground (Hovering, RTK-GPS)	5	7.5	10.5

different confidence level is provided in Table 1. Based on the 802.11ad protocol [43], the SNR for a GPS-based system maps into a PHY-bitrate drop of 17 percent with probability 50 percent and a drop of 33 percent with probability 25 percent compared to static Ground-to-Ground links.

3.4 Summary and Discussion

Below, we highlight the main take-away points from this experimental study that we will directly leverage in our channel model and beam selection algorithm:

- Hovering introduces significant path loss in mmWave bands for highly directional, narrow beamwidths. This loss is dependent on the extent of hovering-related motion artifacts, the antenna radiation patterns, and the possibility of an initial sub-optimal beam selection. This, together with the observed effect the UAV airframe has on signal propagation, motivates the need to create a channel model with a systems-driven approach that can be tailored towards different antenna configurations and UAV hovering characteristics.
- Existing standards for mmWave communication, such as the 802.11ad, are not optimized for best beam alignment in UAV links, and lead to a persistent performance degradation over time. Thus, we need to design a custom beam selection algorithm, which is able to make a better selection at the end of the regular beam-sweeping phase, without modifying the standard.

4 mmWave Channel Model for UAV Links

In this section, we first determine where our contributions are within the channel modelling framework in Section 4.1, where we also discuss the most relevant known results that are leveraged in building comprehensive mmWave models. We then introduce our proposed model in Section 4.2, where we provide a complete estimation of mmWave-band fading that can be applied to multiple UAV hovering scenarios. Table 5 lists all notations and can be found at the end of the document.

4.1 Channel Model Background

In wireless propagation, fading can be classified into large and small scale. Large scale fading accounts for Free Space Path Loss (FSPL) and shadowing effect. Small scale fading includes rapid fluctuations of the received signal strength over very short distance and time, which is manifest through multipath and doppler effect. Our proposed channel model do not intend to provide a more accurate estimation of these effects, but instead, to complement existing channel modelling efforts to obtain an accurate fading estimation tailored to UAV-to-Ground links. In Fig. 8, we show a diagram with the aforementioned classification into large and small scale fading and

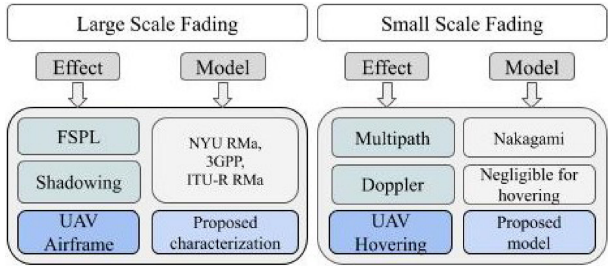

Fig. 8. Contribution within the channel model framework.

the effects belonging to each category. Within this channel modelling framework, we illustrate where our contributions, i.e., UAV airframe and hovering-related effects discussed in Sections 3.2 and 3.3 respectively, fit. In particular, we consider airframe loss L_{Afr} as additional large scale fading and hovering-related loss L_{Hov} as small scale fading, as the latter is caused by the UAV change of location around its targeted coordinates over time. In Fig. 8, we also refer to some of the most relevant models in the literature, that can be jointly combined with our work. In particular, for large scale fading, the NYU Rural Macro environments (RMa) model [18] is a suitable option, since it is specifically derived for mmWave frequencies, obtained through extensive measurements in the 73 GHz band, with accompanying experimental validation. Other alternatives such as the 3GPP and ITU-R RMa path loss models were originally derived for the sub-6 GHz band. Regarding small scale fading due to multipath, Nakagami distribution is an accurate model at mmWave frequencies [44]. Finally, additional path loss due to interference generated by doppler spread is given in [31]. However, doppler effect is typically considered negligible for speeds below 10 m/s, and thus, it is not included for scenarios in which UAVs are hovering at a fixed location.

4.2 Proposed Channel Model for UAV-to-Ground Links

In this section, we introduce our proposed stochastic channel model for estimating additional fading specific to UAV-based links, cumulatively caused by the UAV airframe and hovering-related effects discussed in Section 3. In particular, we consider the airframe effect on the radiation pattern, and the losses caused by beam misalignment and sub-optimal beam selection. The proposed model takes multiple input parameters (Section 4.2.1), to be tailored to the system beamforming training configuration, deployment parameters and hardware assumptions, such as antenna features and level of accuracy of the UAV localization system. We then introduce the steps to build the model in Sections 4.2.3, 4.2.4, and 4.2.5, where we estimate misalignment loss, total hovering-related loss, and total link-loss, as well as the probability that they remain below a given threshold, crucial for accurate link-budget estimation and careful deployment planning.

4.2.1 Input Parameters

In order to provide an accurate fading estimation, our channel model takes the following inputs:

1) *3-D static and aerial antenna radiation patterns*. Our channel model requires both radiation patterns in order to

determine additional loss caused by the UAV airframe L_{Afr} in the angular domain. We build the 3-D radiation patterns from 2-D azimuth θ and elevation φ slices of the antenna power distribution. We obtain the 2-D slices from measurements, as we describe in Section 3.2, as well as through antenna array synthesis with limited accuracy (see Fig. 4). Alternatively, if the antenna dimensions are known, 3-D radiation patterns can be directly obtained in simulation, using electromagnetic software packages.

2) *UAV motion data during hovering*. We collect UAV motion data during the complete flight time, for all translational and rotational types of motion illustrated in Fig. 1. From this data, we build the UAV hovering statistics in Section 4.2.3. To measure translational data, we use a highly accurate low-cost RTK-GPS (EMLID Reach M+).
3) *Beamforming training parameters*. In particular, we consider the angular range evaluated during beam-sweeping $\Delta_{\theta_{SW}}$, $\Delta_{\varphi_{SW}}$, and the angular resolution $\delta_{\theta_{SW}}, \delta_{\varphi_{SW}}$, this is, the angular distance between two consecutive evaluated beams. By considering beamforming training parameters within the model, it is possible to evaluate the effect of different beam-searching reduction techniques extensively proposed in the literature in UAV links, which has been mostly evaluated in static scenarios. We leverage the beamforming parameters and hovering statistics built from the UAV positioning data to estimate the probability for a certain pair of beam to be selected after the beam-sweeping procedure, in Section 4.2.4. This is crucial, as the selection of a particular pair of beams with certain probability, together with the aerial and static antenna radiation patterns, stochastically determine the fading experienced (see Fig. 5).
4) *Deployment parameters*, including the distance between transmitter and receiver d, directly provided or estimated from the UAV and Ground node localization data. Additional fading such as the caused by unfavorable atmospheric conditions or different types of environment can be easily build into the model, as we next illustrate in Section 4.2.2.

4.2.2 A Systems Perspective for Stochastic Fading Estimation

We start by formulating the total link loss or fading L_{Tot} as

$$L_{Tot} = L_{FSPL} + L_{Afr} + L_{Hov}, \tag{1}$$

where, L_{FSPL} is the Free Space Path Loss, L_{Afr} is the fading caused by the effect of the UAV airframe on the antenna radiation pattern and L_{Hov} comprises all hovering-related fading. We separate L_{Hov} into three terms: fading due to an initial sub-optimal beam selection L_{SubOpt}, fading due to distance variations between transmitter and receiver L_{Δ_r}, due to the UAV translational motion along x-axis, and fading caused by beam misalignment L_{Misal} due to translational motion along y and z axes, as well as yaw and pitch.

$$L_{Hov} = L_{SubOpt} + L_{\Delta_r} + L_{Misal}. \tag{2}$$

Notice from Fig. 5b that, for a given pair of beams with transmitter and receiver pointing angular directions $\{\theta_T, \varphi_T\}$ and $\{\theta_R, \varphi_R\}$, L_{SubOpt} is deterministic. We use the notation (u, v) to refer to a specific pair of beams with indexes $u \in \mathbb{N}$ in azimuth and $v \in \mathbb{N}$ elevation dimensions. A deterministic behaviour also applies to L_{FSPL} and L_{Afr}, since the distance d variability during hovering is included in L_{Δ_r}, as part of L_{Hov}, and assumed to be constant for the L_{FSPL} estimation. Thus, by considering the deterministic nature of the aforementioned factors, and noticing that for a fixed pair of beams, $L_{Misal}|_{(u,v)}$ and L_{Δ_r} are the only stochastic terms, we estimate the probability for a given total link fading $L_{Tot}|_{(u,v)}$ as follows:

$$P(L_{Tot}|_{(u,v)}) = P(L_{\Delta_r} + L_{Misal}|_{(u,v)}). \tag{3}$$

Where the sum between L_{Δ_r} and $L_{Misal}|_{(u,v)}$ is related to the total link fading $L_{Tot}|_{(u,v)}$ according to Eqs. (1) and (2)

$$\begin{aligned} L_{\Delta_r} + L_{Misal}|_{(u,v)} = \\ L_{Tot}|_{(u,v)} - L_{FSPL} - L_{Afr} - L_{SubOpt}|_{(u,v)}. \end{aligned} \tag{4}$$

Notice that Eq. (3) assumes the selection of a *given pair* of beams. Therefore, the probability for the UAV-to-Ground link to experience a certain total fading $P(L_{Tot})$ considering *all possible pairs* of beams which are candidate to be selected after the beam-sweeping procedure, depends on (i) the probability for a given pair of beams (u,v) to be selected after the beam sweeping procedure, denoted as $P(u, v)$, as well as (ii) the probability for the link to experience the loss calculated from Eq. (4), denoted as $P(L_{\Delta_r} + L_{Misal}|_{(u,v)})$

$$P(L_{Tot}) = \sum_{u,v} P(u, v) P(L_{\Delta_r} + L_{Misal}|_{(u,v)}). \tag{5}$$

With $\sum_{u,v} P(u, v) = 1$. Then, the estimated average total link fading is given by

$$\overline{L_{Tot}} = L_{FSPL} + L_{Afr} + \overline{L_{Hov}}. \tag{6}$$

With $\overline{L_{Hov}}$ the average hovering-related fading

$$\overline{L_{Hov}} = \overline{L_{\Delta_r}} + \sum_{u,v} (L_{SubOpt}|_{(u,v)} + \overline{L_{Misal}}|_{(u,v)}) \cdot P(u, v). \tag{7}$$

We derive each term in the next sections. Here, we first remark the systems approach taken by this model, as it considers hardware-related loss, as well as beamforming training and deployment parameters. Moreover, the model provides flexibility to include any additional classical fading which is relevant to the scenario under analysis, such as those referenced in Fig. 8. This can be achieved by simply replacing the term L_{FSPL} by more accurate estimations, which include additional fading effects such as shadowing or unfavorable weather conditions, or by directly adding new terms into Eq. (1).

4.2.3 Modeling Motion of Hovering UAVs

The first step towards building our UAV-to-Ground channel model, is to determine the hovering-related loss L_{Hov}. This, together with L_{Afr}, already characterized in Section 3.2,

TABLE 2
UAV to Polar Coordinates Conversion

Polar Coordinates	UAV Coordinates Projection over (r, θ, φ)
Δ_r	$\Delta_{r_{(x)}} = \Delta_x$ $\Delta r_{(y)} = \sqrt{(\Delta y)^2 + d^2} - d \approx 0$ $\Delta r_{(z)} = \sqrt{(\Delta z)^2 + d^2} - d \approx 0$ $\Delta r_{(roll)} = \Delta r_{(pitch)} = \Delta r_{(yaw)} = 0$
Δ_θ	$\Delta_{\theta_{(y)}} = atan(\frac{\Delta_y}{d})$ $\Delta_{\theta_{(yaw)}} = \Delta_{yaw}$ $\Delta_{\theta_{(x)}} = \Delta_{\theta_{(z)}} = \Delta_{\theta_{(roll)}} = \Delta_{\theta_{(pitch)}} = 0$
Δ_φ	$\Delta_{\varphi_{(z)}} = atan(\frac{\Delta_z}{d})$ $\Delta_{\varphi_{(pitch)}} = \Delta_{pitch}$ $\Delta_{\varphi_{(x)}} = \Delta_{\varphi_{(y)}} = \Delta_{\varphi_{(roll)}} = \Delta_{\varphi_{(yaw)}} = 0$

represent fading particular to UAV-links. To this extent, we statistically model all types of UAV motion during hovering and build each motion distribution, similar to the one we show for a single type of motion in Fig. 2. Recalling Fig. 1, hovering motion manifests in longitudinal, lateral, and vertical translational displacements along (x, y, z) axes, as well as rotational displacements around them, respectively, denoted as *roll*, *pitch*, and *yaw*.

It is important to notice that not all types of motion are independent from each other. For instance, UAV translational displacement along the negative side of y-axis $-\Delta_y$, can be compensated by positive rotational displacement around z-axis $+\Delta_{yaw}$. Similar dependency exists between Δ_z and Δ_{pitch}. For this reason, it is desirable to define UAV displacements in a coordinate system which enables to jointly combine the effect of different types of motion. We select the polar coordinate system (r, θ, φ), where $r \equiv x$, $\theta \equiv yaw$ is the rotational dimension in the plane XY, and $\varphi \equiv pitch$ is the rotational dimension in the plane YZ, see Fig. 7b. Moreover, with the selection of the polar coordinate system, we directly relate UAV displacements with the antenna radiation pattern, naturally characterized in azimuth θ and elevation φ, required for estimating hovering-related loss. The distance between transmitter and receiver is defined along dimension r. In Table 2, we provide the conversion from UAV to polar coordinates, according to Fig. 7b. The notation $\Delta_{i_{(j)}}$ represents the projection of the hovering displacement for the UAV coordinate j over the polar dimension i. Accordingly, hovering displacements in polar coordinates are given by

$$\Delta_r \approx \Delta_x \tag{8}$$

$$\Delta_\theta = \Delta_{\theta_{(y)}} + \Delta_{yaw} = atan\left(\frac{\Delta_y}{d}\right) + \Delta_{yaw} \tag{9}$$

$$\Delta_\varphi = \Delta_{\varphi_{(z)}} + \Delta_{pitch} = atan\left(\frac{\Delta_z}{d}\right) + \Delta_{pitch}. \tag{10}$$

In order to characterize the UAV motion comprehensively, we collect experimental hovering data during flight

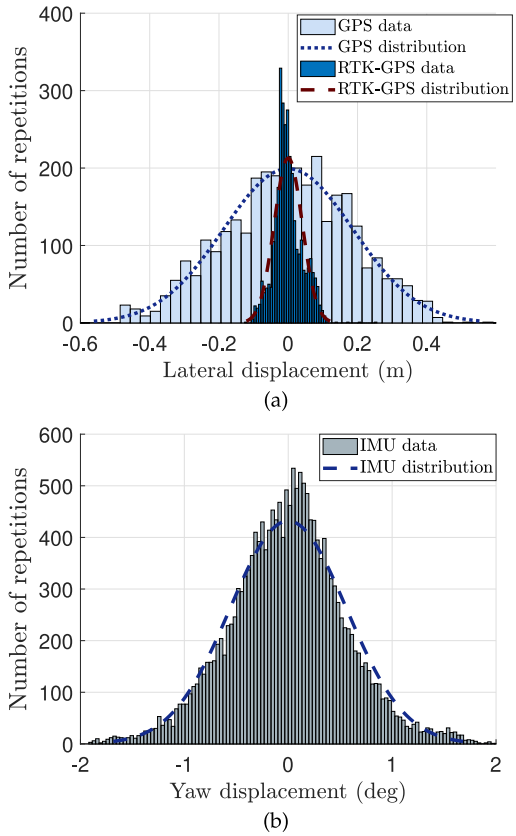

Fig. 9. Gaussian distribution of UAV (a) translational displacements in y-axis and (b) rotational displacement in yaw.

for all six types of motion in Fig. 1. We perform our experiments under typical hovering conditions, i.e., scenarios with no buildings within a radius of 15 meters, strong satellite signal reception (SNR >35 dB) from at least 4 satellites, and maximum wind speed of 17 miles/hour, which are conducive for safe and reliable operation. We measured translational displacement in (x,y,z) coordinates with two different hardware configurations, for the M600 UAV navigation system relying on (i) GPS and (ii) a high-cost RTK-GPS, which limits the UAV maximum hovering displacement, and thus, its variance. For both configurations, we used a separate low-cost RTK-GPS system, mounted on the UAV with the only purpose of accurate data logging, not interacting with the UAV navigation system; thereby, not affecting its flight pattern. For both configurations, we collected rotational displacement data using IMU sensors.

Fig. 9a and 9b show the distribution of the experimental data collected for Δ_y and Δ_{yaw} respectively, as examples. From the experimental data collected, we observe that UAV displacements during hovering follow a Gaussian distribution in each UAV coordinate j:

$$\Delta_j \sim \mathcal{N}(\mu_{\Delta_j}, \sigma^2_{\Delta_j}), \tag{11}$$

where $\sigma^2_{\Delta_j}$ represents the variance of the displacement and μ_{Δ_j} its mean value, tending to the targeted coordinates at which the UAV ideally should be located. Placing the origin of the UAV coordinate system at the targeted coordinates, we set $\mu_{\Delta_j} = 0, \forall j$ for simplicity. In Table 3, we provide specific values for the variance of the data collected. The hovering statistics used in this work are not pre-determined and

TABLE 3
Variance of Hovering Displacement

Navigation system	$\sigma^2_{\Delta_x}$	$\sigma^2_{\Delta_y}$	$\sigma^2_{\Delta_z}$	$\sigma^2_{\Delta_{roll}}$	$\sigma^2_{\Delta_{pitch}}$	$\sigma^2_{\Delta_{yaw}}$
GPS	*0.0586*	*0.035*	*0.0582*	*0.1968*	*0.1876*	*0.0027*
RTK-GPS	*0.0032*	*0.0021*	*0.0033*	*0.1415*	*0.1139*	*0.0028*

fixed. Instead, we build these statistics from measurements collected during live deployment, as UAV hardware choices, and operating conditions may be different for specific use cases.

Next, from the characterization performed in UAV coordinates, we build the hovering distribution in polar dimensions. According to Eq. (8), the probability density function (PDF) for the displacement in the radial dimension $f_r(\Delta_r)$ is approximated by the Gaussian PDF of the longitudinal displacement $\Delta_x \sim \mathcal{N}(0, \sigma^2_{\Delta_x})$. Moreover, according to Eq. (9), the PDF for the displacement in the azimuth dimension $f_\theta(\Delta_\theta)$ needs to consider the combined effect of *yaw* as well as the projection over θ of the translational displacements along y-axis $\Delta_{\theta_{(y)}}$. We define the unnormalized distribution for the azimuth displacement as

$$f_{\theta_{\mathcal{U}}}(\Delta_\theta) = \int_{-\pi}^{\pi}\int_{-\pi}^{\pi} f(\Delta_{\theta_{(y)}}) f(\Delta_{yaw}) \delta(\Delta_\theta - \Delta_{\theta_{(y)}} - \Delta_{yaw}) d_{\Delta_{yaw}} d_{\Delta_{\theta_{(y)}}}, \tag{12}$$

where $f(\Delta_{\theta_{(y)}})$ and $f(\Delta_{yaw})$ are the independent Gaussian PDFs of $\Delta_{\theta_{(y)}}$ and Δ_{yaw} respectively, and δ is the Dirac delta function

$$\delta(\Delta_\theta) = \begin{cases} 1, & if\ \Delta_\theta = \Delta_{\theta_{(y)}} + \Delta_{yaw} \\ 0, & otherwise. \end{cases} \tag{13}$$

The PDF for the azimuth displacement $f_\theta(\Delta_\theta)$ is calculated in Eq. (14) by normalizing $f_{\theta_{\mathcal{U}}}(\Delta_\theta)$, and represents the probability for $\Delta_\theta = \Delta_{\theta_{(y)}} + \Delta_{yaw}, \forall \Delta_{\theta_{(y)}}, \Delta_{yaw} \in [-\pi, \pi]$, in order to account for possible compensation in θ.

$$f_\theta(\Delta_\theta) = \frac{f_{\theta_{\mathcal{U}}}(\Delta_\theta)}{\int_{-\pi}^{\pi} f_{\theta_{\mathcal{U}}}(\Delta_\theta) d_{\Delta_\theta}}. \tag{14}$$

The PDF for the displacement in the elevation dimension $f_\varphi(\Delta_\varphi)$, is likewise obtained from Eqs. (12), (13), and (14), by replacing Δ_{yaw} by Δ_{pitch} and $\Delta_{\theta_{(y)}}$ by the projection over φ of the translational displacement along z-axis $\Delta_{\varphi_{(z)}}$, as per Eq. (10).

4.2.4 Modelling Fading for Sub-Optimal Beam Selection

In Fig. 7a, we showed that the motion experienced by hovering UAVs may cause the selection of sub-optimal pair of beams when beam-sweeping procedure completes. Further, in Fig. 5b, we illustrated how the selection of a certain pair of beams determines (i) the loss at the center of the hovering displacement range $L_{SubOpt}|_{(u,v)}$, as the addition of L_{Tx} and L_{Rx}, and (ii) the range of values of the antenna gain utilized for transmission and reception as the UAV hovers during the complete flight time. For these reasons, given the high dependence of fading on the particular pair of beam selected, the next step towards building our proposed channel model is to determine the set of candidate pair of beams in azimuth and elevation dimensions to which transmitter and receiver may point, post beam-sweeping. To do so, we do not assume that $\{\theta_T, \varphi_T\}$ for transmitter and $\{\theta_R, \varphi_R\}$ for receiver are independent from each other. Instead, we consider that for a particular beam $\{\theta_T, \varphi_T\}$, only a subset of all possible $\{\theta_R, \varphi_R\}$ can achieve alignment between transmitter and receiver, which also depends on UAV hovering motion. Thus, we determine the subset of all possible combinations of $\{(\theta_T, \theta_R), (\varphi_T, \varphi_R)\}$ which are candidate pair of beams.

Moreover, as illustrated in Fig. 2, alignment and thus, beam selection occurs when both transmitter and receiver point to the same angular direction, e.g., both to the same $+\theta$ for the azimuth dimension, as they are located facing each other. Thus, we define the subset of candidate pair of beams indexes as $\mathcal{S} = \{u, v\}$, associated to $\{\theta_u, \varphi_v\}$ equal for transmitter and receiver, with $u \in \{1, \ldots, U\}, v \in \{1, \ldots, V\}$, where U, V are the number of candidate angular directions in θ and φ dimensions respectively, and $N_b = U \cdot V$, the total number of candidate pair of beams evaluated. The set of possible candidates $\mathcal{S}$ depends on (i) the beamforming training parameters, (Section 4.2.1) and shown in Fig. 7b, and (ii) the hovering conditions and the distance between transmitter and receiver, jointly characterized through $f_\theta(\Delta_\theta), f_\varphi(\Delta_\varphi)$ (Section 4.2.3). Thus, given the stochastic nature of hovering, we need to determine the probability for each candidate pair of beams $(u, v) \in \mathcal{S}$ to be selected, in order to provide an accurate loss estimation.

To this extent, we first determine the PDF for the ground receiver node to direct its beam toward a certain angular direction $f_R(\theta)$. For a static case, this term only depends on the angular distribution determined by the beamforming training parameters $f_{R_{SW}}(\Delta_{\theta_{SW}}, \delta_{\theta_{SW}})$, and is given by

$$f_R(\theta) = f_{R_{SW}}(\Delta_{\theta_{SW}}, \delta_{\theta_{SW}}) = \begin{cases} \frac{1}{U}, & if\ \theta = p \cdot \delta_{\theta_{SW}}, \forall \theta \in \Delta_{\theta_{SW}} \\ 0, & \text{otherwise.} \end{cases} \tag{15}$$

With $p \in \mathbb{Z}$. We similarly determine $f_R(\varphi)$ in the elevation dimension considering $\Delta_{\varphi_{SW}}$, $\delta_{\varphi_{SW}}$ and replacing U by V. Moreover, the probability for the UAV transmitter node to direct its beam toward a certain angle $f_T(\theta)$ is jointly determined by the distribution given the beamforming training parameters at the transmitter side $f_{T_{SW}}(\Delta_{\theta_{SW}}, \delta_{\theta_{SW}})$ and the UAV hovering distribution $f_\theta(\Delta_\theta)$. We formally define its unnormalized distribution as

$$f_{T_{\mathcal{U}}}(\theta) = \int_{-\pi}^{\pi}\int_{-\pi}^{\pi} f_{T_{SW}}(\theta_{SW}) f_\theta(\Delta_\theta) \delta(\theta - \theta_{SW} - \Delta_\theta) d_{\Delta_\theta} d_{\theta_{SW}}. \tag{16}$$

Where δ was defined in Eq. (13), and the normalized version of Eq. (16), $f_T(\theta)$, is obtained similar to Eq. (14). We could further generalize this analysis by considering transmitter and receiver beamforming training parameters to be different from each other, by simply using different $\Delta_{\theta_{SW}}, \delta_{\theta_{SW}}$ values in Eqs. (15) and (16). Next, we estimate the probability for a given pair of sub-optimal beams to be selected after beam-sweeping from the following PDF:

$$f_{SubOpt}(\theta,\varphi)=\frac{f_T(\theta)f_R(\theta)f_T(\varphi)f_R(\varphi)}{\int_{-\pi}^{\pi}\int_{-\pi}^{\pi}f_T(\theta)f_R(\theta)f_T(\varphi)f_R(\varphi)d_\varphi d_\theta}. \quad (17)$$

Where the aforementioned dependency between candidate beams has been included, only considering those candidate beams that meet $\theta=\theta_{Tx}=\theta_{Rx}$. Then, the probability for a certain pair of beams (u,v) to be selected after beam-sweeping is given by

$$P(u,v)=\int_{\theta_u-\theta_\Gamma}^{\theta_u+\theta_\Gamma}\int_{\varphi_v-\varphi_\Gamma}^{\varphi_v+\varphi_\Gamma}f_{SubOpt}(\theta,\varphi)d_\varphi d_\theta. \quad (18)$$

Where $\theta_\Gamma=\frac{\theta_{u+1}-\theta_u}{2},\varphi_\Gamma=\frac{\varphi_{v+1}-\varphi_v}{2}$. Moreover, we formulate the fading caused by the selection of a sub-optimal pair of beams (u,v) according to Fig. 5b, as

$$L_{SubOpt}|_{(u,v)}=L_{Tx}(\theta_u)+L_{Rx}(\theta_u)+L_{Tx}(\varphi_v)+L_{Rx}(\varphi_v). \quad (19)$$

Where each fading term is directly obtained from the 3-D aerial h_a and static h_s radiation patterns. To illustrate this process, we set forth the following example. First, the fading term at the transmitter side for the candidate beam u in the azimuth dimension, denoted as $L_{Tx}(\theta_u)$, is calculated as the difference between the transmitter (aerial) antenna radiation pattern h_a evaluated at θ_u, and the radiation pattern maximum value. Notice that the radiation pattern maximum values in θ and φ dimensions correspond to the antenna broadside directions θ_{bs},φ_{bs}, i.e., the maximum of the radiation pattern, normal to the axis of the array, as we show in Fig. 5b. Following this, we estimate the fading terms in Eq. (19) as:

$$L_{Tx}(\theta_u)=h_a(\theta_{bs})-h_a(\theta_u) \quad (20a)$$

$$L_{Rx}(\theta_u)=h_s(\theta_{bs})-h_s(\theta_u) \quad (20b)$$

$$L_{Tx}(\varphi_v)=h_a(\varphi_{bs})-h_a(\varphi_v) \quad (20c)$$

$$L_{Rx}(\varphi_v)=h_s(\varphi_{bs})-h_s(\varphi_v). \quad (20d)$$

With the formulation provided in this section, we are now able to estimate the fading caused by a sub-optimal beam selection L_{SubOpt}, for a given pair of beams (u,v) within the 3-D space, which is selected with a probability dictated by $f_{SubOpt}(\theta,\varphi)$.

4.2.5 Modelling Fading for Beam Misalignment

In order to provide a stochastic total link fading estimation, we recall to Section 4.2.2. In particular, in Eq. (3), we justified that, estimating the probability for the link to experience a total fading given the selection of a pair of beams after beam-sweeping $P(L_{Tot}|_{(u,v)})$, is reduced to estimating the probability of the sum between misalignment loss and translational displacement along the radial dimension $P(L_{\Delta_r}+L_{Misal}|_{(u,v)})$, by exploiting the deterministic nature of every other fading term involved. Thus, in order to estimate $P(L_{Tot}|_{(u,v)})$, we first define the joint distribution for beam misalignment as

$$f_{Misal}(\Delta_\theta,\Delta_\varphi)=f_{\Delta_\theta}(\Delta_\theta)f_{\Delta_\varphi}(\Delta_\varphi). \quad (21)$$

Where $f_{\Delta_\theta}(\Delta_\theta),f_{\Delta_\varphi}(\Delta_\varphi)$ are the PDFs for the UAV hovering displacement in azimuth and elevation characterized in Section 4.2.3, assumed to be independent from each other. The probability for a given misalignment loss $P(L_{Misal}|_{(u,v)})$ can be directly obtained by integrating Eq. (21). Then, we estimate the probability for a certain $L_{Tot}|_{(u,v)}$ as

$$P(L_{Tot}|_{(u,v)})=\iint\limits_{\Omega_{(\Delta_r,\Delta_\theta,\Delta_\varphi)}}f_{Misal}(\Delta_\theta,\Delta_\varphi)f_r(\Delta_r)d_{\Delta_r}d_{\Delta_\varphi}d_{\Delta_\theta}. \quad (22)$$

With

$$\Delta_r\in[-\infty,\infty],\quad \Delta_\theta,\Delta_\varphi\in[-\pi,\pi],\quad \Omega_{(\Delta_r,\Delta_\theta,\Delta_\varphi)}\subset C.$$

Where C is the set containing all possible combinations of UAV displacements in the radial, azimuth and elevation dimensions $\{(\Delta_r,\Delta_\theta,\Delta_\varphi)\}$ and Ω is the subset of C such that the loss term $L_{\Delta_r}+L_{Misal}|_{(u,v)}$ for the subset of displacements considered meets Eq. (4) for a given $L_{Tot}|_{(u,v)}$ value. The loss term L_{Δ_r} is due to small variations on the distance between transmitter and receiver as the UAV hovers, causing path loss fluctuations given by

$$L_{\Delta_r}(dB)=10\cdot log\left(\frac{d+\Delta_r}{d}\right)^2. \quad (23)$$

Moreover, misalignment loss is caused by displacements in the θ and φ dimensions given a particular pair of beams $L_{Misal}|_{(u,v)}$, and is directly obtained from the static and aerial 3-D antenna radiation patterns. The calculation is similar to Eqs. (20a), (20b), (20c), and (20d), with the particularity that misalignment loss is not calculated as additional loss compared to the broadside direction θ_{bs}, but instead, compared to the angular direction for the specific pair of beams selected (θ_u,φ_v)

$$L_{Tx}(\Delta_\theta)=h_a(\theta_u)-h_a(\theta_u+\Delta_\theta) \quad (24a)$$

$$L_{Rx}(\Delta_\theta)=h_s(\theta_u)-h_s(\theta_u+\Delta_\theta) \quad (24b)$$

$$L_{Tx}(\Delta_\varphi)=h_a(\varphi_v)-h_a(\varphi_v+\Delta_\varphi) \quad (24c)$$

$$L_{Rx}(\Delta_\varphi)=h_s(\varphi_v)-h_s(\varphi_v+\Delta_\varphi). \quad (24d)$$

We then have

$$L_{\Delta_\theta}|_{(u,v)}=L_{Tx}(\Delta_\theta)+L_{Rx}(\Delta_\theta) \quad (25)$$

$$L_{\Delta_\varphi}|_{(u,v)}=L_{Tx}(\Delta_\varphi)+L_{Rx}(\Delta_\varphi). \quad (26)$$

Which together determine the 3-D misalignment loss

$$L_{Misal}|_{(u,v)}=L_{\Delta_\theta}|_{(u,v)}+L_{\Delta_\varphi}|_{(u,v)}. \quad (27)$$

Notice that in contrast to Eqs. (20a), (20b), (20c), and (20d), where (θ_u,φ_v) remained constant for a particular pair of beams, here $(\Delta_\theta,\Delta_\varphi)$ vary over time as the UAV hovers.

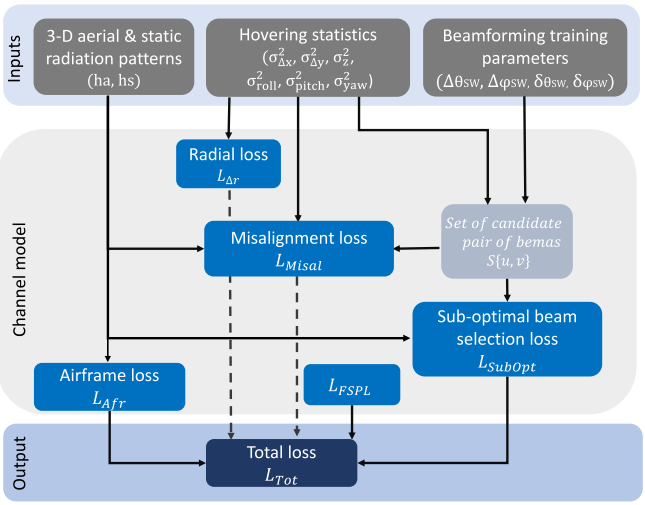

Fig. 10. Channel model flow diagram.

Then, the probability for $L_{Misal}|_{(u,v)}$ to be below a certain threshold γ_{th} is defined as

$$P(L_{Misal}|_{(u,v)} \leq \gamma_{th}) = \int\int_{\Omega_{(\Delta_\theta,\Delta_\varphi)}} f_{Misal}(\Delta_\theta, \Delta_\varphi) d_{\Delta_\varphi} d_{\Delta_\theta}. \quad (28)$$

With

$$\Omega_{(\Delta_\theta,\Delta_\varphi)} = \{(\Delta_\theta, \Delta_\varphi)\}/L_{\Delta_\theta}|_{(u,v)} + L_{\Delta_\varphi}|_{(u,v)} \leq \gamma_{th}.$$

And $P(L_{Tot}|_{(u,v)} \leq \gamma_{th})$ can be similarly obtained from Eq. (22) considering $P(L_{\Delta_r} + L_{Misal}|_{(u,v)}) \leq \gamma_{th})$.

Additionally, we estimate the average total link fading $\overline{L_{Tot}}$ and average hovering fading $\overline{L_{Hov}}$ given in Eqs. (7) and (6) from (i) the probability for a certain pair of beams to be selected after beam-sweeping, $P(u,v)$, given in Eq. (18), (ii) the fading caused by a sub-optimal beam selection, $L_{SubOpt}|_{(u,v)}$, given in Eq. (19), and (iii) the averaged beam misalignment fading $\overline{L_{Misal}}|_{(u,v)}$ and the average loss caused by translational displacement along the radial dimension $\overline{L_{\Delta_r}}$ given by

$$\overline{L_{Misal}}|_{(u,v)} = \sum_{\Delta_\theta,\Delta_\varphi} (L_{\Delta_\theta}|_{(u,v)} + L_{\Delta_\varphi}|_{(u,v)}) \cdot P(\Delta_\theta)P(\Delta_\varphi)) \quad (29)$$

$$\overline{L_{\Delta_r}} = \sum_{\Delta_r} L_{\Delta_r} \cdot P(\Delta_r). \quad (30)$$

Where $P(\Delta_r), P(\Delta_\theta)P(\Delta_\varphi)$ can be obtained by directly integrating the PDFs derived in Section 4.2.3, and $\sum_{\Delta_\theta,\Delta_\varphi}(P(\Delta_\theta)P(\Delta_\varphi)) = \sum_{\Delta_r} P(\Delta_r) = 1$. Finally, for completeness, we define $\overline{L_{\Delta_\theta}}$ and $\overline{L_{\Delta_\varphi}}$ as

$$\overline{L_{\Delta_\theta}}|_{(u,v)} = \sum_{\Delta_\theta} L_{\Delta_\theta}|_{(u,v)} \cdot P(\Delta_\theta) \quad (31)$$

$$\overline{L_{\Delta_\varphi}}|_{(u,v)} = \sum_{\Delta_\varphi} L_{\Delta_\varphi}|_{(u,v)} \cdot P(\Delta_\varphi). \quad (32)$$

Fig. 10 illustrate a channel model flow diagram which all inputs and dependencies considered. The model proposed here is leveraged in Section 5, where we present an algorithm to diminish hovering-related loss caused by a sub-optimal beam selection. Specifically, we apply this model in the upcoming Eqs. (36), (37), and (38), in order to estimate the link loss in all three dimensions θ, φ and r.

5 Algorithm for Beam Optimization in UAVs

In Fig. 7a and 7c we experimentally demonstrated the large additional fading compared to static scenarios that the selection of a sub-optimal pair of beam introduces, highly degrading the SNR at the receiver. Motivated by this, we next develop an algorithm to find a near-to-optimum pair of beams, alternative to the standard, with the goal of enhancing the average SNR at the receiver, and thus, the mmWave communication link performance.

5.1 Algorithm Intuition

A major cause for link performance degradation is the selection of a pair of beams whose performance is evaluated when the UAV location is close to the boundaries of its hovering displacement range (*Location 1* in Fig. 2). Thus, even though the selected pair of beams achieves the highest performance over all candidate pairs at that location, the tendency of the UAV to move back to the most likely hovering region (*Location 2* in Fig. 2), results in strong beam misalignment in average, for the selected pair of beams.

Our proposed algorithm prevents this situation by allocating *weights* to the measured received power, for every candidate pair considered during beam-sweeping. The weights $w \in [0,1]$ are given according to the particular UAV location within the hovering range in which each pair of beams performance is determined. This is, pair of beams evaluated at different locations have distinct w values. With this approach, we aim to quantify trough w the likelihood that a hovering UAV stays at the location in which the performance of each pair of beams is measured, being $w = 1$ the highest. Thus, taking the example in Fig. 2, w values tend to 1 for those pairs evaluated close to *Location 1*, and tend to 0 for those pairs evaluated in the surroundings of *Location 2*. Notice that w serves as a stochastic confidence metric of the frequency for transmitter and receiver to be aligned over time, and thus, to provide their maximum antenna gains. Given w dependency on the UAV location, its value is conditioned by the hovering statistics, and in particular, by the angular and radial displacements $\{\Delta_r, \Delta_\theta, \Delta_\varphi\}$ already characterized in Section 4.2.3.

5.2 Relative Time Scales Magnitude

In this section, we introduce the concept of temporal scale, in order to provide an algorithmic solution applicable to diverse types of systems. We start by defining the *time scale magnitude* as the complete time-span the sounders take to perform beam-sweeping and evaluate the link performance for all pair of beams. In the WiFi standard 802.11ad, this process takes up to 30 ms, being lower in the 802.11ay release [45]. During such time, the UAV transmitter change of location is negligible, given the long time-span effect of hovering. We denote this condition as Small Temporal Scale (STS). Notice that under STS conditions, w value remains the same for every pair of beams, as they are all evaluated at

the same UAV location. We however, chose to extend the algorithm evaluation to a generic case, in which the transmitter location may randomly vary during the beam-sweeping time, and within the hovering maximum displacement range. We denote this condition as Large Temporal Scale (LTS). To evaluate our work performance under LTS conditions, we operate beam-sweeping within a time-span of 2 minutes. During this time, different subsets of beams within the angular beam-sweeping range $\Delta\theta_{SW}$ are evaluated every few seconds.

Notice that LTS is a generalized case of STS conditions, where the UAV location changes over time, and thus, different pair of beams have different w values. Thus, we focus on LTS scenarios, and demonstrate that, even under the most generic conditions, our algorithm is still capable of determining a near-to-optimum pair of beams.

5.3 Formulating Confidence-Cost Weights

Given the w dependence on the UAV hovering displacements, discussed in Section 5.1, we formulate w as a function of the PDF in the radial dimension calculated from Eqs. (8) and (11), as well as the PDFs in the azimuth and elevation dimensions obtained from Eqs. (12), (13), and (14), as follows:

$$w_k(\Delta_r) = \frac{f_r(\Delta_{r_k})}{f_r(\Delta_r = \mu_{\Delta_r})} \tag{33}$$

$$w_k(\Delta_\theta) = \frac{f_\theta(\Delta_{\theta_k})}{f_\theta(\Delta_\theta = \mu_{\Delta_\theta})} \tag{34}$$

$$w_k(\Delta_\varphi) = \frac{f_\varphi(\Delta_{\varphi_k})}{f_\varphi(\Delta_\varphi = \mu_{\Delta_\varphi})}. \tag{35}$$

With $k \in \{1, \dots N_b\}$ and N_b the total number of pair of beams evaluated. According to this definition, let us consider a pair of beams k that was evaluated during beam-sweeping close to the center of the hovering displacement range in r and θ dimensions, $\Delta_{rk} \approx \mu_{\Delta_r}$, $\Delta_{\theta k} \approx \mu_{\Delta_\theta}$, but close to the boundaries of the hovering displacement range in φ dimension $\Delta_{\varphi_k} \approx \mu_{\Delta_\varphi} + 3\sigma^2_{\Delta_\varphi}$. Then, w_k values according to Eqs. (33), (34), and (35) are $w_k(\Delta_r), w_k(\Delta_\theta) \approx 1$ and $w_k(\Delta_\theta) \approx 0$, showing high *confidence* for the UAV to remain at the radial and azimuth locations in which the pair of beams k was evaluated during beam-sweeping, and low *confidence* to remain at its elevation location.

Notice that the previous formulation gives the same relevance to w in all three dimensions (r, θ, φ) However, not all types of displacements in (r, θ, φ) cause the same degree of fading. Specifically, in Section 3.3, we experimentally proved that displacements in θ and φ dimensions cause fading of up to 30 dB due to a sub-optimal beam selection as well as beam misalignment, highly related to the 3-D antenna radiation patterns. On the contrary, displacements along the radial dimension only cause fading fluctuations lower than 1 dB for the typical hovering conditions we specified in Section 4.2.3. Therefore, we adjust w_k according to the averaged fading expected in each dimension as follows:

$$w_{L_k}(\Delta_r) = w_k(\Delta_r) \cdot \left(1 - \frac{\overline{L_{\Delta_r k}}}{\overline{L_{hov_k}}}\right) \tag{36}$$

$$w_{L_k}(\Delta_\varphi) = w_k(\Delta_\theta) \cdot \left(1 - \frac{\overline{L_{\Delta_\theta k}}}{\overline{L_{hov_k}}}\right) \tag{37}$$

$$w_{L_k}(\Delta_\varphi) = w_k(\Delta_\varphi) \cdot \left(1 - \frac{\overline{L_{\Delta_\varphi k}}}{\overline{L_{hov_k}}}\right). \tag{38}$$

Where $\overline{L_{hov_k}} = \overline{L_{\Delta_r k}} + \overline{L_{\Delta_\theta k}} + \overline{L_{\Delta_\varphi k}}$, and these last three terms are derived in Eqs. (30), (31) and (32). By doing so, the weights w_{L_k}, include a stochastically determined *cost* related to the probability for the UAV to suffer from fading in each dimension, if the pair of beams k is selected. This *cost*, together with degree of *confidence*, jointly determine the near-to-optimum pair of beams k^*, ensuring high average performance.

5.4 Algorithm Formulation and Execution

Algorithm 1. Near-to-Optimum Beam Selection Under Hovering Conditions

Input: $(pow)_{k \leftarrow ts}, k = 1 \dots N_b$, N_b pairs evaluated
Input: $(x, y, z)_{m \leftarrow ts} \leftarrow (lat, long, alt)_{m \leftarrow ts}, m = 1 \dots M$, M GPS-RTK measurements collected during t_{Sweep}
Output: $k^*, \quad k \in [1 \dots N_b]$
1. Build ts-mapping matrix $M \in \mathbb{R}^{2 \times N_b}$
$H = [(pow)_{k \leftarrow ts}; (x, y, z)_{k \leftarrow ts}]$
2. Compute hovering statistics from $(x, y, z)_m \forall m$
$f_r(\Delta_r) \approx f(x - \mu_x)$
$f_\theta(\Delta_\theta) \approx f(atan(\frac{y - \mu_y}{d}))$
$f_\varphi(\Delta_\varphi) \approx f(atan(\frac{z - \mu_z}{d}))$
3. Compute expected losses $\overline{L_{\Delta_r k}}, \overline{L_{\Delta_\theta k}}, \overline{L_{\Delta_\varphi k}}$ as in Eqs. (30), (31), and (32)
4. Compute weights $w_k(\Delta_r), w_k(\Delta_\theta), w_k(\Delta_\varphi)$ from Eqs. (33), (34), and (35)
5. Adjust weights $w_{L_k}(\Delta_r), w_{L_k}(\Delta_\theta), w_{L_k}(\Delta_\varphi)$ from Eqs. (36), (37), and (38)
6. Find:
$k^* = max_k\{pow_k w_{L_k}(\Delta_r) + pow_k w_{L_k}(\Delta_\theta) + pow_k w_{L_k}(\Delta_\varphi)$

Algorithm 1 presents the execution flow of our proposed method in an actual experiment. The algorithm requires as inputs the received power from the mmWave sounder units, as well as UAV localization data. During the standard beam-sweeping, the sounder units generate time-stamped (ts) power measurements for each of the N_b pair of beams evaluated (Algorithm 1, input 1), which are forwarded to the central computer through a control channel by an Ethernet link. In addition, the RTK-GPS EMLID Reach M+ stores the time-stamped M coordinate samples collected for the complete beam-sweeping time t_{Sweep}, as the UAV hovers (input 2). Once beam-sweeping is completed, we access localization data from the host computer through a WiFi link and convert it from geographic (latitude, longitude, altitude) to UTM (Universal Transverse Mercator) coordinates (x, y, z). Then, through the time-stamps, we associate the power measurement for each pair of beams pow_k with the UAV coordinates at the evaluation instant, generating a resultant mapping matrix H (step 1). From the UAV coordinates data collected over t_{Sweep}, we build the UAV hovering statistics (step 2). We use these, together with the static and aerial antenna radiation patterns, to find the estimated

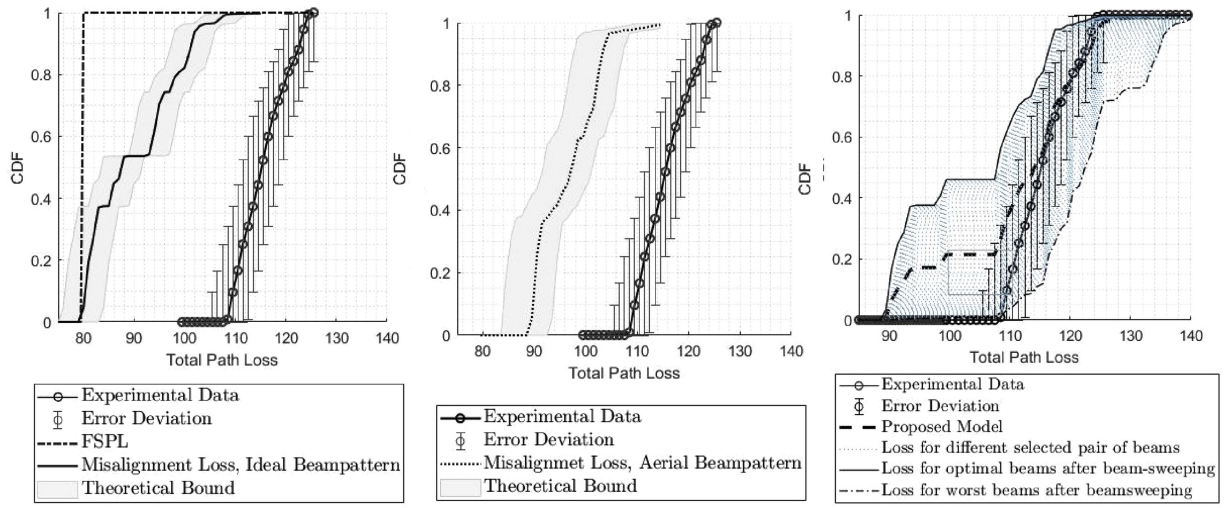

(a) FSPL and Ideal-Hovering model (b) Aerial-Hovering model (c) Proposed model

Fig. 11. Empirical validation of existing and proposed channel models. Experimental data collected over 10 minutes is compared with (a) the FSPL and Ideal-Hovering models, (b) the Aerial-Hovering model and (c) the Proposed model.

losses for each dimension r, θ, φ (step 3), and eventually, the weights for each pair of beams w_k (steps 4, 5). We apply the resultant weights to the measured power for each pair pow_k (step 6), and select the near-to-optimum pair of beams as

$$k^* = max_k\{pow_k w_{L_k}(\Delta_r) + pow_k w_{L_k}(\Delta_\theta) + pow_k w_{L_k}(\Delta_\varphi)\}. \tag{39}$$

Note that k^* is optimal only in a static case, where there is no UAV hovering-related motion. With hovering and STS conditions, w_{L_k} values are equal for all N_b pair of beams in each dimension, and k^* is selected only based on pow_k, same as the standard. However, notice that if the one location where all N_b pairs are evaluated differs from the center of the UAV hovering displacement distribution in any of the three dimensions, k^* is still sub-optimal in average under STS conditions. In this case, a better pair can be chosen by exploiting the hovering stochastic distributions provided by our model. In a more general case, under LTS conditions, in which each pair of beams is evaluated at different locations, finding the optimum pair is not always feasible, since there is no guarantee that perfect alignment occurs within t_{Sweep}. In this case, k^* given by Eq. (39) is a near-to-optimum solution, i.e., the best possible solution given the available data.

6 Experimental Results

We first provide experimental validation for the analytical channel model formulated in Section 4, using data collected during UAV actual flights, in Section 6.1. In this section, we also provide simulation results for multiple scenarios using the model. Then, in Section 6.2, we experimentally demonstrate the performance gain achieved with the proposed beam selection algorithm presented in Section 5. Our setup here is similar to the description provided in Section 3.3.2 and illustrated in Fig. 6, consisting of a TG sounder unit mounted on a M600 DJI UAV, acting as transmitter, and a second unit as static ground receiver. Only for the results presented in Fig. 15, the transmitter is mounted on a mobile slider in order to emulate the UAV hovering motion without battery constraints. All other results were obtained under actual flight.

6.1 Channel Model Validation

In order to validate the fading estimation provided by our channel model, we establish a UAV-to-Ground link with the setup in Fig. 6. Once the UAV is hovering during actual flight, we perform beam-sweeping and fix the best pair of beams for transmission, according to the standard. We maintain the selected pair over the remaining UAV flight time ($\approx$ 10 minutes). From the experimental data collected, we build the Cumulative Distribution Function (CDF) of the UAV-to-Ground link path loss, in Fig. 11. The error deviation of the experimental data is a hardware-specific feature, with a value of up to 4 dB. Alongside with it, we provide the estimated path loss using different analytical channel models. In particular, in Fig. 11a we consider (i) the *FSPL model*, which only accounts for frequency and distance between transmitter and receiver and (ii) the *Misalignment Loss, Ideal Beampattern* model, in which we include the ideal antenna radiation pattern with a beamwidth of $2.8°$, shown in Fig. 4, as well as power fluctuations caused by beam misalignment, estimated through real hovering data collected over time during the experiment. The latter model comes closest to existing works in the literature [31], in which the authors only account for misalignment loss and the main

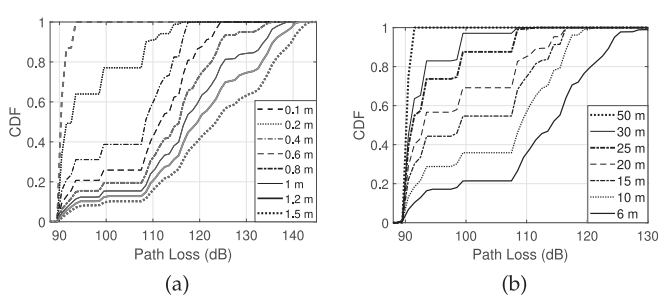

(a) (b)

Fig. 12. Total fading with (a) hovering and (b) distance.

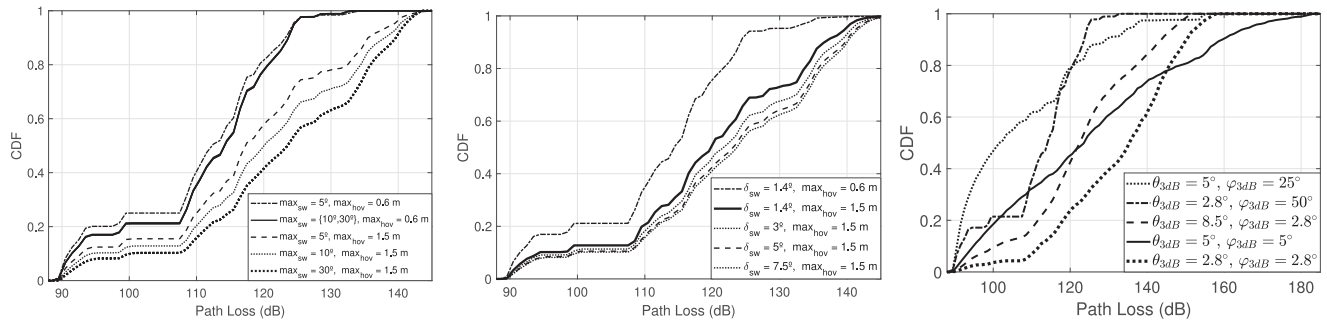

Fig. 13. Total fading for different (a) beam-sweeping angular range and hovering conditions, (b) beam-sweeping angular resolution and hovering conditions and (c) 3-D radiation patterns.

lobe of an ideal antenna radiation pattern, neglecting the effect of secondary side lobes.

In addition, in Fig. 11b we present the estimated path loss using (iii) the *Misalignment Loss, Aerial Beampattern* model, in which we replace the ideal radiation pattern in the previous model by the 3-D aerial radiation pattern in Fig. 14b, built from the aerial 2-D azimuth slice in Fig. 4, and a 2-D elevation slice with $\theta_{3dB} = 50^{\circ}$ built in simulation using antenna array synthesis. Thus, in this model, we account for L_{Afr}, additional losses caused by the UAV airframe. We include theoretical bounds for the analytical models, estimated by considering an error of 20 percent on the typical deviation for the hovering statistical distributions. This provides a fair comparison between models if insufficient hovering data is collected, given the UAV battery constraints, or under the presence of anomalies during data collection. Lastly, in Fig. 11c, we present the path loss estimation given by (iv), our *Proposed Model*. This, in addition to misalignment loss and realistic 3-D aerial and static radiation patterns, includes the effect of sub-optimal beam selection after beam-sweeping. Specifically, we include the estimated loss for each candidate pair of beams (dashed blue lines), stochastically determined by a Monte Carlo simulation, as well as their averaged value. Notice that our *Proposed Model* provides the closest estimation to the experimentally measured path loss, which is seen as a particular realization of the probabilistic estimation we provide. Moreover, the results presented here clearly reveal the accuracy gain achieved when the effect of each UAV-related fading component discussed so far, is added to the model. In particular, our model drops estimation error to ≈ 0.2 percent, approximately 18x lower than the *Misalignment Loss, Ideal Beampattern* model, the closest to the state-of-the-art models existing in the literature. Next, we use our UAV-to-Ground channel model in order to estimate the total fading L_{Tot} in a 60 GHz link for multiple scenarios. In Fig. 12a, we present simulation results for the CDF of the total path loss, tailored to different maximum UAV hovering displacements, considered to be equal in θ and φ dimensions. For all cases in Fig. 12a, we set the distance between transmitter and receiver to $d = 6\ m$. In Table 4, we provide the UAV hovering statistics used for this simulation. In addition, we include the hovering statistics for a case of $d = 20m$. In Fig. 12b we estimate the total link path loss for different d values. We observe how additional link fading is encountered as UAV hovering displacement grows and distance shrinks.

In Fig. 13a and 13b, we present simulation results for different beamforming training parameters and two different UAV hovering displacements, 0.6 and 1.5 m, respectively representing typical and strong hovering conditions. From Fig. 13a, path loss increases as the maximum angular ranges evaluated during beam-sweeping $\Delta\theta_{SW} = \Delta\varphi_{SW}$ grow (max_{SW} in the figure). This is expected, since for large $\Delta\theta_{SW}, \Delta\varphi_{SW}$ values, the selected pair of beams can potentially be further from the antenna main lobe (broadside direction). Moreover, as maximum hovering displacement

TABLE 4
Hovering Parameters for Fig. 12a

Maximum displacement $\approx 3\sigma_{\Delta_x} = 3\sigma_{\Delta_y}$	$\sigma^2_{\Delta_x}$	$\sigma^2_{\Delta_{\theta_y}}\|_{d=6m}$	$\sigma^2_{\Delta_{\theta_y}}\|_{d=20m}$
0.1 m	$1.09{\cdot}10^{-3}$	$3.08{\cdot}10^{-5}$	$2.78{\cdot}10^{-6}$
0.2 m	$4.36{\cdot}10^{-3}$	$1.23{\cdot}10^{-4}$	$1.11{\cdot}10^{-5}$
0.4 m	0.0177	$4.84{\cdot}10^{-4}$	$4.44{\cdot}10^{-5}$
0.6 m	0.04	$1.09{\cdot}10^{-3}$	$9.99{\cdot}10^{-5}$
0.8 m	0.07	$1.93{\cdot}10^{-3}$	$1.77{\cdot}10^{-4}$
1 m	0.11	$3.03{\cdot}10^{-3}$	$2.77{\cdot}10^{-4}$
1.5 m	0.25	$8.31{\cdot}10^{-2}$	$2.5{\cdot}10^{-2}$

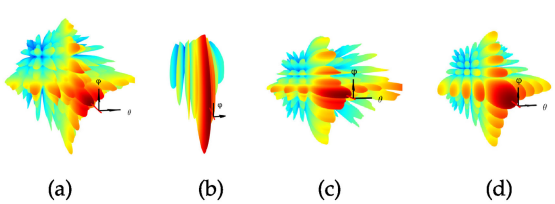

Fig. 14. 3-D normalized radiation patterns with $\{\theta_{3dB}, \varphi_{3dB}\}$: (a) $\{2.8^{\circ}, 2.8^{\circ}\}$, (b) $\{2.8^{\circ}, 50^{\circ}\}$, (c) $\{2.8^{\circ}, 8.5^{\circ}\}$ and (d) $\{5^{\circ}, 5^{\circ}\}$.

Fig. 15. Initial tests with sounder Tx mounted on slider.

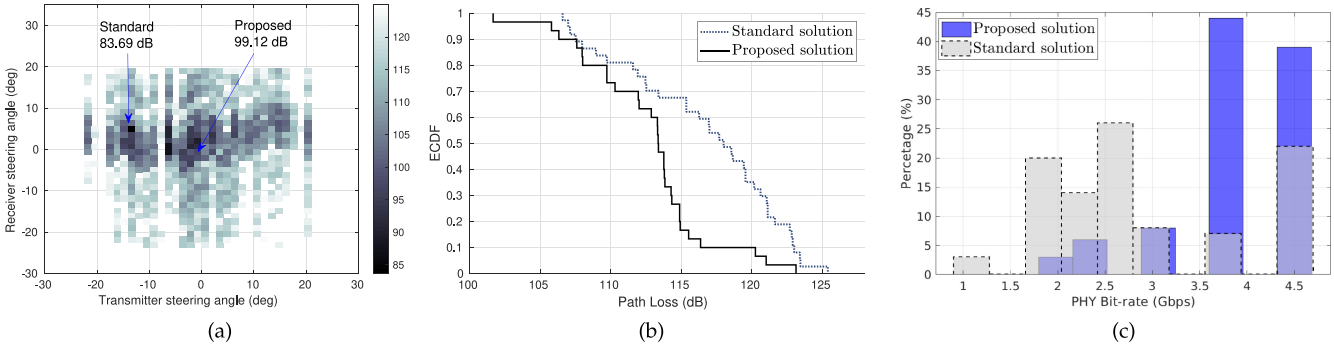

Fig. 16. Experimental results for UAV tests showing a comparison between standard and proposed algorithm in terms of (a) measured path loss during beam-sweeping and selected beams, (b) path loss for selected beams and (c) PHY bit-rate.

(max_{hov} in the figure) becomes more severe, chances for sub-optimal beam selection increase, leading to a worst average link performance. In addition, from Fig. 13b, we observe that path loss decreases with the angular beamforming resolution δ_{SW}.

In Fig. 14 we present different 3-D radiation patterns created from real measurements in an anechoic chamber (cases of 2.8° and 8.5°) and simulation (all other beamwidths). The estimated path loss considering different radiation patterns in presented in Fig. 13c. This results show a tendency for the link to suffer from greater path loss, as beamwidth narrows.

6.2 beam Selection Validation

In order to validate our beam selection algorithm, we compare the average performance achieved with our proposed pair of beams and the pair of beams selected by the standard. We remark here that, during actual UAV experiments, we need to evaluate both solutions within a single battery-determined UAV flight-time (≈12 minutes). This prevents vibrations during taking-off and landing from altering relative location between transmitter and receiver and hovering patterns, providing a fair comparison between both solutions. Thus, we perform a two-step validation process, by using two different setups: (i) with the transmitter sounder mounted on a mobile slider that we remotely control in order to emulate the random UAV lateral displacements during hovering without the UAV battery constraint, shown in Fig. 15 and (ii), during actual UAV flights with the setup shown in Fig. 6. For both setups, once the UAV is in hovering motion, we perform beam-sweeping followed by beam selection according to the 802.11ad standard. We maintain the selected pair of beams for half the UAV flight-time. We then find a near-to-optimum pair of beams according to Algorithm 1, and fix it for the second half of the UAV flight-time. The two inputs required by the algorithm according to Section 5.4 are the measured power obtained from the mmWave sounder units, and the UAV localization data obtained from the low-cost RTK-GPS.

For the first setup, in Fig. 17a we show a comparison between the standard and the proposed solution in terms of the path loss ECDF. Our proposed solution limits the average path loss by 8.7 dB. It does so by selecting a pair of beams evaluated at the center of the UAV hovering displacement range, even though it presented lower performance during the standard-defined beam-sweeping. In Fig. 17b, we present a comparison in terms of PHY bit-rate. With our selected pair of beams, the bit-rate is constant at its maximum value, since path loss fluctuations are not sufficient to decrease the modulation order [43], in contrast to the standard-defined solution.

In Fig. 16a, 16b, and 16c we introduce results for our second setup, from an actual UAV flight. For this test, we initially locate transmitter and receiver facing each other, and thus, the optimum pair of beams is expected to be close to the antenna broadside directions ($\theta_{bs} = \varphi_{bs} = 0°$) for both sounders. In Fig. 16a, we present the measured path loss for all transmitting and receiving steering angles evaluated during beam-sweeping. Additionally, we highlight the pair of beams selected by the standard and the proposed algorithm. As expected, the standard selects the pair of beams with lowest path loss during evaluation, which is 83.69 dB. However, their angles (-14.1° for transmitter and 5.6° for receiver) are far from the expected broadside angular direction. In contrast, our proposed algorithm selects a different pair of beams in spite of their higher path loss of 99.12 dB during beam-sweeping evaluation, steering toward -2.8°, both transmitter and receiver. This selection is driven by the trade-off between (i) the higher path loss measured during beam-sweeping, (ii) the more centered UAV location in (r, θ, φ) dimensions within the hovering displacement range, and (iii) the effect the displacement in each dimension has on the expected average total link fading. In Fig. 16b, we compare the path loss experienced using our proposed pair of beams and the one provided by the standard. Our solution achieves an average path loss reduction of 4 dB. In Fig. 16c, we compare the PHY bit-rate for both solutions. In this case, our

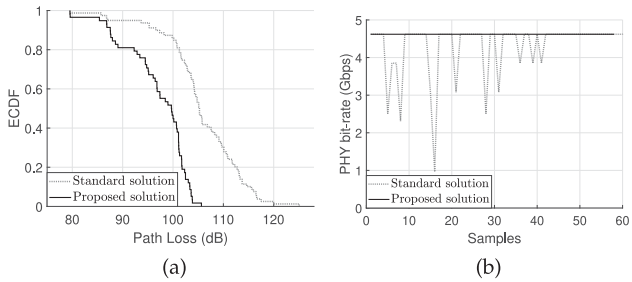

Fig. 17. Performance comparison between beam selected by standard and proposed algorithm for slider test in terms of (a) path loss and (b) PHY bit-rate.

TABLE 5
Table of Notations

Symbol	Description
List of Acronyms	
TG	Terragraph
AWV	Antenna Weight Vector
RTK	Real-Time Kinematic
IMU	Inertial Measurement Unit
$EIRP$	Effective Isotropic Radiated Power
$ECDF$	Empirical Cumulative Distribution Function
$PHY-bitrate$	Physical layer bitrate
SNR	Signal-to-Noise Ratio
Tx, Rx	Transmitter, Receiver
Antenna Parameters	
θ	Azimuth
φ	Elevation
$\theta_{3dB}, \varphi_{3dB}$	3-dB beamwidth in azimuth, elevation
$\theta_{bs}, \varphi_{bs}$	Broadside direction in azimuth, elevation
E	Electric field
Z_0	Free-space impedance
P_d	Power density
g	Antenna gain
P_r	Received power
h_a	Aerial radiation pattern (UAV)
h_s	Static radiation pattern (Ground)
Beamforming Training Parameters	
$\Delta_{\theta_{SW}}, \Delta_{\varphi_{SW}}$	Beam-sweeping angular range
$\delta_{\theta_{SW}}, \delta_{\varphi_{SW}}$	Beam-sweeping angular resolution
UAV Hovering Model Parameters	
j	UAV coordinate $\{x, y, z, roll, pitch, yaw\}$
i	Polar coordinate$\{r, \theta, \varphi\}$
Δ_j, Δ_i	Hovering displacement in dimensions i, j
$\Delta_{i_{(j)}}$	Projection of displacement in coord. j over i
μ_{Δ_j}	Mean vale of displacement in j
$\sigma^2_{\Delta_j}$	Variance of displacement in j
$f(\Delta_j)$	PDF of displacement in i
$f_i(\Delta_i)$	PDF of displacement in j
$f_{ul}(\Delta_i)$	Unnormalized PDF of displacement in i
$\delta(\Delta_i)$	Dirac delta function for displacement in i
Channel Model Parameters	
d	Distance between transmitter and receiver
L_{FSPL}	Free Space Path Loss
L_{Afr}	UAV airframe-related loss
L_{Hov}	Hovering-related loss
L_{SubOpt}	Sub-optimal beam selection loss
L_{Misal}	Beam misalignment loss
L_{Δ_r}	Distance d fluctuation loss
L_{Tot}	Total link loss
θ_T, φ_T	Transmitter steering angles
θ_R, φ_R	Receiver steering angles
$f_T(\theta), f_T(\varphi)$	Tx PDF to sweep in certain angle
$f_R(\theta), f_R(\varphi)$	Rx PDF to sweep in certain angle
$f_{T_{SW}}$	Tx steering PDF given beamforming
$f_{R_{SW}}$	Rx steering PDF given beamforming
u, v	Candidate beam indices in θ and φ
U, V	Total candidate beams in θ and φ
S	Subset of candidate beams (u, v)
N_b	Total combination of candidate beams
$L_{Tx}(\theta_u), L_{Tx}(\varphi_v)$	L_{SubOpt} at transmitter given pair (u, v)
$L_{Tx}(\Delta_\theta), L_{Tx}(\Delta_\varphi)$	L_{Misal} for hovering displacements $\Delta_\theta, \Delta_\varphi$
L_{Δ_i}	Loss caused by UAV displacement in i
C	Set of all possible combinations of Δ_i
Ω	Subset of C causing a given loss
γ_{th}	Threshold for stochastic loss estimation
Algorithm Parameters	
$w_k(\Delta_i)$	Confidence weight, pair k, dimension i
$w_{L_k}(\Delta_i)$	Confidence-cost weight, pair k, dimension i
pow_k	Measured power pair of beams k
ts	Time-stamped
t_{sweep}	Beam-sweeping time
M	Location samples collected during t_{sweep}
H	Mapping matrix $(pow_k, UAV_{x,y,z})$
k^*	Proposed pair of beams

proposed solution maintains a high bit-rate above 3 Gbps for the 91 percent of the measurements taken during evaluation, compared to 37 percent achieved by the standard.

We highlight here that the performance gain achieved with our proposed algorithm varies for each particular realization given its stochastic nature, and it is highly dependent on the hovering pattern, UAV hardware, beam-sweeping training configuration and deployment parameters. From our experimental results, our solution guarantees at least the same performance as the standard, providing a significant average gain when hovering prevents the standard from determining the optimal beam selection.

7 Conclusion

In this paper, we demonstrate the important issues impacting UAV communications in the 60 GHz mmWave band, in particular those arising from the UAV airframe and the UAV continuous motion during hovering. For the latter, we quantify the effect of beam misalignment and the sub-optimal beam selection encountered when performing conventional beam-sweeping in real UAV scenarios. We build a stochastic analytical channel model to estimate the total path loss in an UAV-to-Ground link, which can be tailored to different UAV hardware, 3-D antenna radiation patterns, beamforming training parameters and deployment conditions. Moreover, driven by the sub-optimal beam selection problem encountered during our experiments, we propose a low-complexity standard-compliant algorithm in order to enhance the average link performance. Overall, we consider that adopting a systems-level approach is the key to provide accurate fading estimations. This includes (i) the effect of the UAV airframe on the antenna radiation pattern, which causes significant fading, (ii) the impact of a sub-optimal beam selection after beam-sweeping, and (iii) power fluctuations caused by beam misalignment, whose magnitude depends on the sub-optimal beam selected as well as on the transmitting and receiving 3-D radiation patterns. We experimentally validate both the channel model and our beam selection algorithm with 802.11ad complaint Terragraph sounder units mounted on DJI M600 UAVs.

Acknowledgments

This work was supported by the Office of Naval Research under grant N000141612651. The Terragraph Channel Sounders used for the experiments in this paper are the part of the Facebook Connectivity initiative.

References

[1] F. Zhou, M. Y. Naderi, K. Sankhe, and K. Chowdhury, "Making the right connections: Multi-AP association and flow control in 60 GHz band," in *Proc. IEEE Conf. Comput. Commun.*, 2018, pp. 1214–1222.

[2] Facilitate America's superiority in 5G technology (5G FAST) plan, Federal Communications Commission, Accessed: Apr. 27, 2020. [Online]. Available: https://docs.fcc.gov/public/attachments/DOC-354326A1.pdf

[3] C. Zhang, W. Zhang, W. Wang, L. Yang, and W. Zhang, "Research challenges and opportunities of UAV millimeter-wave communications," *IEEE Wireless Commun.*, vol. 26, no. 1, pp. 58–62, Feb. 2019.

[4] T. Banerjee, K. R. Chowdhury, and D. P. Agrawal, "Using polynomial regression for data representation in wireless sensor networks," *Int. J. Commun. Syst.*, vol. 20, no. 7, pp. 829–856, 2007.

[5] Z. Xiao, P. Xia, and X.-G. Xia, "Enabling UAV cellular with millimeter-wave communication: Potentials and approaches," *IEEE Commun. Mag.*, vol. 54, no. 5, pp. 66–73, May 2016.
[6] M. Mozaffari, W. Saad, M. Bennis, and M. Debbah, "Efficient deployment of multiple unmanned aerial vehicles for optimal wireless coverage," *IEEE Commun. Lett.*, vol. 20, no. 8, pp. 1647–1650, Aug. 2016.
[7] A. Trotta, M. Di Felice, F. Montori, K. R. Chowdhury, and L. Bononi, "Joint coverage, connectivity, and charging strategies for distributed UAV networks," *IEEE Trans. Robot.*, vol. 34, no. 4, pp. 883–900, Aug. 2018.
[8] G. Secinti, P. B. Darian, B. Canberk, and K. R. Chowdhury, "Resilient end-to-end connectivity for software defined unmanned aerial vehicular networks," in *Proc. IEEE 28th Annu. Int. Symp. Pers. Indoor Mobile Radio Commun.*, 2017, pp. 1–5.
[9] J. Kim and A. F. Molisch, "Enabling Gigabit services for IEEE 802.11ad-capable high-speed train networks," in *Proc. IEEE Radio Wireless Symp.*, 2013, pp. 145–147.
[10] T. Nitsche, A. B. Flores, E. W. Knightly, and J. Widmer, "Steering with eyes closed: Mm-Wave beam steering without in-band measurement," *Proc. IEEE Conf. Comput. Commun.*, 2015, pp. 2416–2424.
[11] T. Nitsche, C. Cordeiro, A. B. Flores, E. W. Knightly, E. Perahia, and J. C. Widmer, "IEEE 802.11ad: Directional 60 GHz communication for multi-Gigabit-per-second Wi-Fi [Invited Paper]," *IEEE Commun. Mag.*, vol. 52, no. 12, pp. 132–141, Dec. 2014.
[12] L. Zhu, J. Zhang, Z. Xiao, X. Cao, D. O. Wu, and X.-G. Xia, "3D beamforming for flexible coverage in millimeter-wave UAV communications," *IEEE Wireless Commun. Lett.*, vol. 8, no. 3, pp. 837–840, Jun. 2019.
[13] H. Safi, A. Dargahi, and J. Cheng, "Spatial beam tracking and data detection for an FSO link to a UAV in the presence of hovering Q3 fluctuations," *Elect. Eng. Syst. Sci. Signal Process.*, 2019, *arXiv: 1904.03774*.
[14] MATRICE 600 UAV specifications, Accessed: Apr. 01, 2020. [Online]. Available: https://www.dji.com/es/matrice600/info
[15] S. Geng, J. Kivinen, X. Zhao, and P. Vainikainen, "Millimeter-wave propagation channel characterization for short-range wireless communications," *IEEE Trans. Veh. Technol.*, vol. 58, no. 1, pp. 3–13, Jan. 2009.
[16] J. Huang, C.-X. Wang, R. Feng, J. Sun, W. Zhang, and Y. Yang, "Multi-frequency mmWave massive MIMO channel measurements and characterization for 5G wireless communication systems," *IEEE J. Sel. Areas Commun.*, vol. 35, no. 7, pp. 1591–1605, Jul. 2017.
[17] D. He, L. Wang, K. Guan, B. Ai, J. Kim, and Z. Zhong, "Channel characterization for mmWave vehicle-to-infrastructure communications in urban street environment," in *Proc. 13th Eur. Conf. Antennas Propag.*, 2019, pp. 1–5.
[18] G. R. MacCartney and T. S. Rappaport, "Rural macrocell path loss models for millimeter wave wireless communications," *IEEE J. Sel. Areas Commun.*, vol. 35, no. 7, pp. 1663–1677, Jul. 2017.
[19] T. S. Rappaport, Y. Xing, G. R. MacCartney, A. F. Molisch, E. Mellios, and J. Zhang, "Overview of millimeter wave communications for fifth-generation (5G) wireless networks–With a focus on propagation models," *IEEE Trans. Antennas Propag.*, vol. 65, no. 12, pp. 6213–6230, Dec. 2017.
[20] T. Abbas, F. Qamar, I. Ahmed, K. Dimyati, and M. B. Majed, "Propagation channel characterization for 28 and 73 GHz millimeter-wave 5G frequency band," in *Proc. IEEE 15th Student Conf. Res. Develop.*, 2017, pp. 297–302.
[21] J. Blumenstein, J. Vychodil, M. Pospisil, T. Mikulasek, and A. Prokes, "Effects of vehicle vibrations on mm-Wave channel: Doppler spread and correlative channel sounding," in *Proc. IEEE 27th Annu. Int. Symp. Pers. Indoor Mobile Radio Commun.*, 2016, pp. 1–5.
[22] X. Cai *et al.*, "Low altitude UAV propagation channel modelling," in *Proc. IEEE 11th Eur. Conf. Antennas Propag.*, 2017, pp. 1443–1447.
[23] W. Khawaja, I. Guvenc, and D. Matolak, "UWB channel sounding and modeling for UAV air-to-ground propagation channels," in *Proc. IEEE Global Commun. Conf.*, 2016, pp. 1–7.
[24] D. W. Matolak and R. Sun, "Unmanned aircraft systems: Air-ground channel characterization for future applications," *IEEE Veh. Technol. Mag.*, vol. 10, no. 2, pp. 79–85, Jun. 2015.
[25] W. Khawaja, I. Guvenc, D. W. Matolak, U.-C. Fiebig, and N. Schneckenberger, "A survey of air-to-ground propagation channel modeling for unmanned aerial vehicles," *IEEE Commun. Surveys Tuts.*, vol. 21, no. 3, pp. 2361–2391, Thirdquarter 2019.
[26] G. E. Athanasiadou and G. V. Tsoulos, "Path loss characteristics for UAV-to-ground wireless channels," in *Proc. IEEE 13th Eur. Conf. Antennas Propag.*, 2019, pp. 1–4.
[27] E. Greenberg, A. Bar, and E. Klodzh, "Los classification of UAV-to-ground links in built-up areas," in *Proc. IEEE Int. Conf. Microwaves Antennas Commun. Electron. Syst.*, 2019, pp. 1–5.
[28] P. S. Bithas, V. Nikolaidis, A. G. Kanatas, and G. K. Karagiannidis, "UAV-to-ground communications: Channel modeling and UAV selection," *IEEE Trans. Commun.*, early access, May 4, 2020, doi: 10.1109/TCOMM.2020.2992040.
[29] W. Khawaja, O. Ozdemir, and I. Guvenc, "UAV air-to-ground channel characterization for mmWave systems," in *Proc. IEEE 86th Veh. Technol. Conf.*, 2017, pp. 1–5.
[30] R. Kovalchukov *et al.*, "Analyzing effects of directionality and random heights in drone-based mmWave communication," *IEEE Trans. Veh. Technol.*, vol. 67, no. 10, pp. 10064–10069, Oct. 2018.
[31] M. T. Dabiri, H. Safi, S. Parsaeefard, and W. Saad, "Analytical channel models for millimeter wave UAV networks under hovering fluctuations," *Elect. Eng. Syst. Sci. Signal Process.*, 2019, *arXiv: 1905.01477*.
[32] D. Steinmetzer, D. Wegemer, M. Schulz, J. Widmer, and M. Hollick, "Compressive millimeter-wave sector selection in off-the-shelf IEEE 802.1 lad devices," in *Proc. 13th Int. Conf. Emerg. Netw. Experiments Technol.*, 2017, pp. 414–425.
[33] S. Q. Zhang, H. T. Kung, and Y. Gwon, "InferBeam: A fast beam alignment protocol for millimeter-wave networking," *Comput. Sci. Netw. Internet Architecture*, 2018.
[34] J. Palacios, D. De Donno, and J. Widmer, "Tracking mm-Wave channel dynamics: Fast beam training strategies under mobility," in *Proc. IEEE Conf. Comput. Commun.*, 2017, pp. 1–9.
[35] W. Xu, F. Gao, S. Jin, and A. Alkhateeb, "3D scene based beam selection for mmWave communications," *Elect. Eng. Syst. Sci. Signal Process.*, 2019, *arXiv: 1911.08409*.
[36] M. S. Sim, Y.-G. Lim, S. H. Park, L. Dai, and C.-B. Chae, "Deep learning-based mmWave beam selection for 5G NR/6G with sub-6 GHz channel information: Algorithms and prototype validation," *IEEE Access*, vol. 8, pp. 51 634–51 646, 2020.
[37] Y. Wang, A. Klautau, M. Ribero, A. C. Soong, and R. W. Heath, "MmWave vehicular beam selection with situational awareness using machine learning," *IEEE Access*, vol. 7, pp. 87 479–87 493, 2019.
[38] Terragraph by Facebook. Solving the urban bandwidth challenge, Accessed: May 31, 2020. [Online]. Available: https://terragraph.com
[39] DJI D-RTK GNSS with DATALINK PRO 900 (GPS + BDS), Accessed: Apr. 27, 2020. [Online]. Available: https://www.bhphotovideo.com/c/product/1379999-REG/dji_cp_sb_000376_mat rice_d_rtk_ground_system.html
[40] RTK GNSS reach module for UAV mapping, Accessed: Apr. 01, 2020. [Online]. Available: https://emlid.com/reach/#specifications
[41] S. Hur, T. Kim, D. J. Love, J. V. Krogmeier, T. A. Thomas, and A. Ghosh, "Millimeter wave beamforming for wireless backhaul and access in small cell networks," *IEEE Trans. Commun.*, vol. 61, no. 10, pp. 4391–4403, Oct. 2013.
[42] J. Verbeke and S. Debruyne, "Vibration analysis of a UAV multirotor frame," in *Proc. ISMA Int. Conf. Noise Vibration Eng.*, 2016, pp. 2401–2409.
[43] X. Zhu, A. Doufexi, and T. Kocak, "Beamforming performance analysis for OFDM based IEEE 802.11 ad millimeter-wave WPANs," in *Proc. 8th Int. Workshop Multi-Carrier Syst. Solutions*, 2011, pp. 1–5.
[44] N. Goddemeier and C. Wietfeld, "Investigation of air-to-air channel characteristics and a UAV specific extension to the rice model," in *Proc. IEEE Globecom Workshops*, 2015, pp. 1–5.
[45] P. Zhou *et al.*, "IEEE 802.11 ay-based mmWave WLANs: Design challenges and solutions," *IEEE Commun. Surveys Tuts.*, vol. 20, no. 3, pp. 1654–1681, Thirdquarter 2018.

Sara Garcia Sanchez received the BS and MS degrees in electrical engineering from the Universidad Politecnica de Madrid, Spain, in 2016 and 2018 respectively. She is currently working toward the PhD degree in the Department of Electrical and Computer Engineering, Northeastern University, Boston, Massachusetts, under the guidance of Prof. Kaushik Roy Chowdhury. Her research interests include mmWave, UAV communications, MIMO and optimization techniques.

Subhramoy Mohanti received the MS degree from Northeastern University, Boston, Massachusetts, in 2016. He is currently working toward the PhD degree at the Department of Electrical and Computer Engineering, Northeastern University, Boston, Massachusetts. He is the recipient of the IEEE INFOCOM Best Paper Award (2018) and the Northeastern University Graduate Dissertation Research Grant (2015). His current research interests include UAV networking and communication, wireless protocols, networks, scheduling and optimization techniques.

Dheryta Jaisinghani (Member, IEEE) received the master's degree in information technology (specialization: networking and communication) from the International Institute of Information Technology, Bangalore, India, in 2012, and the PhD degree in computer science (specialization: WiFi networks) from the Indraprastha Institute of Information Technology, Delhi, India, in 2019. She is a postdoctoral research associate in Next Generation Networks and Systems (GENESYS) lab at Northeastern University, Boston, Massachusetts. Her research interests include the areas of pervasive and ubiquitous computing with particular focus on networked systems, large-scale WiFi networks, software-defined-networks, and mobile computing. She is a recipient of the Institute Gold Medal for overall performance during her masters. She has worked as a visiting researcher with LiveLabs, Singapore Management University, Singapore, in 2017. She interned at Arista Networks (then Airtight Networks), in 2014. Before her research career, she was working as a software engineer in Accenture Services Private Limited from 2008-2010.

Kaushik Roy Chowdhury (Senior Member, IEEE) received the MS degree from the University of Cincinnati, Cincinnati, Ohio, in 2006, and the PhD degree from the Georgia Institute of Technology, Atlanta, Georgia, in 2009. He is currently a professor at the Electrical and Computer Engineering Department and assoc. director of the Institute for the Wireless IoT. He was a winner of the Presidential Early Career Award for Scientists and Engineers (PECASE), in 2017, ONR Director of Research Early Career Award, in 2016 and the NSF CAREER Award, in 2015. His current research interests include deep learning for wireless sensing and spectrum access, networked robotics, wireless RF energy harvesting/transfer, and IoT applications for intra/on-body communication.